

# Bayesian inversion for paleogeographic reconstruction and analysis

Ian R. Rose<sup>1</sup>, Yiming Zhang<sup>1</sup>, Nicholas L. Swanson-Hysell<sup>1\*</sup>

<sup>1</sup> Department of Earth and Planetary Science, University of California, Berkeley, CA, USA

\* Correspondence to: swanson-hysell@berkeley.edu

*This manuscript has been prepared for submission to Journal of Geophysical Research: Solid Earth.*

## <sup>1</sup> Abstract

Apparent polar wander paths (APWPs) synthesized from paleomagnetic poles provide the most direct data for reconstructing past paleogeography and plate motions for times earlier than ca. 200 Ma. In this contribution, we describe a new method for APWP synthesis that extends the paleomagnetic Euler pole analysis of Gordon et al. (1984) by placing it within the framework of a Bayesian inverse problem. This approach allows uncertainties in both pole position and age to be incorporated into the synthesis—uncertainties that are often ignored in standard treatments. The paleomagnetic Euler poles resulting from the inversions provide estimates for total plate motion and associated uncertainty. The method allows for inverting for one or more Euler poles with the timing of changepoints from one Euler pole to another being solved as part of the inversion. We show several example inversions on simple synthetic data to demonstrate the capabilities of the method. We illustrate application of the method to constrain rapid rates of motion for cratonic North America associated with the Keweenawan Track of late Mesoproterozoic paleomagnetic poles. We also apply the method to the Cenozoic database of Australia paleomagnetic poles which can be compared to independent plate reconstructions developed using seafloor data. A two Euler pole inversion for the Cenozoic Australia record recovers the northward acceleration of Australia in the Eocene with rates that are consistent with the independent global plate motion models. The application of Markov chain Monte Carlo methods to estimate paleomagnetic Euler poles has the potential to open new directions in quantitative paleogeography.

## <sup>20</sup> Introduction

Plate tectonics is the motion of near-rigid blocks of lithosphere across the surface of Earth, separated by relatively narrow regions of deformation in spreading centers, transform faults, and subduction zones. The relative rigidity of plates means that the motion of most of Earth's surface can be described by a set of Euler poles which specify the position (in latitude and longitude) of a rotation axis and a rate of rotation about this axis for a given plate (cf. Cox and Hart, 2009). Individual points on a plate undergoing rigid rotation are described by small circle paths (Fig. 1).

Euler poles are widely used for describing plate motions due to their simplicity and compactness (e.g. DeMets et al., 2010; Argus et al., 2011). Plate motions have a tendency to

29 remain constant, or approximately so, over time scales of millions to tens of millions of years  
30 (Iaffaldano et al., 2012). This consistency of motion can be seen physically expressed in the shape  
31 of oceanic fracture zones and in hotspot tracks across the lithosphere. These features form gently  
32 curving arcs over large portions of Earth's surface that can be well described by small circles,  
33 consistent with finite Euler rotations of the plate for an extended period of time. As such, the  
34 combination of an Euler pole plus a time interval for which it is active (often called a "stage  
35 pole") is a convenient description of plate motions through Earth history.

36 As the stage pole description of plate motions is a convenient way of reconstructing plate  
37 tectonic history, it is widely used in both continental reconstruction (e.g. Boyden et al., 2011) and  
38 in geodynamical modeling (e.g. McNamara and Zhong, 2005; Bull et al., 2014). Most  
39 reconstructions of plate motions over the past 200 million years rely heavily on fitting Euler pole  
40 rotations to oceanic fracture zones, hotspot tracks, seafloor magnetic isochrons, and, to a lesser  
41 extent, paleomagnetic data (Muller et al., 1993; Seton et al., 2012; Müller et al., 2016). However,  
42 as we look further back in Earth history, many of the records on which these plate tectonic  
43 reconstructions rely largely disappear due to the subduction of oceanic lithosphere. Given the  
44 lack of ocean crust older than  $\sim$ 200 Ma, the paleomagnetic record from continental rocks is the  
45 dominant remaining data. These paleomagnetic data can be used in conjunction with geological  
46 data that provides information on the tectonic setting of plate margins, as well as additional  
47 information such as the correlation of geologic terranes, to develop paleogeographic  
48 reconstructions.

49 It is more challenging to reconstruct past plate motions from paleomagnetic pole positions than  
50 from data derived from oceanic lithosphere for a number of reasons, including: (1) the data are  
51 often sparser; (2) traditional paleomagnetic analysis constrains paleolatitude and the orientation  
52 of a continental block, but does not constrain paleolongitude without additional assumptions; and  
53 (3) paleomagnetic poles can have appreciable uncertainty in both position and age.

54 Gordon et al. (1984) noted that progressions of paleomagnetic poles (which are commonly  
55 referred to as apparent polar wander paths; APWPs) have arcing trajectories similar to fracture  
56 zones and hotspot tracks. This similar geometry is expected given that they are also tracking  
57 plate motion (Fig. 1). Following Francheteau and Sclater (1969), they therefore suggested fitting  
58 small circles to paleomagnetic poles tracks, which would furnish Euler poles for the plate in  
59 question for that time period. This approach for constraining APWPs, called paleomagnetic  
60 Euler pole analysis, has the attractive feature of providing a complete description of the plate  
61 motion, including paleolongitudinal changes and therefore rates of motion. However, it has the  
62 drawback of not providing readily computed uncertainties associated with the paleomagnetic  
63 poles and not incorporating age uncertainties. With some notable exceptions (e.g. Bryan and  
64 Gordon, 1986; Beck, 1989; Tarling and Abdeldayem, 1996; Beck and Housen, 2003; Smirnov and  
65 Tarduno, 2010), paleomagnetic Euler pole analysis has not seen wide adoption.

66 In this contribution, we extend paleomagnetic Euler pole analysis by placing it within a  
67 Bayesian statistical framework and demonstrate how to invert for paleomagnetic Euler poles using  
68 Markov chain Monte Carlo (MCMC) methods. This framework has the advantage of naturally  
69 incorporating uncertainties in paleomagnetic pole positions, as well as widely disparate age  
70 uncertainties associated with individual paleomagnetic poles. The resulting stage poles from these

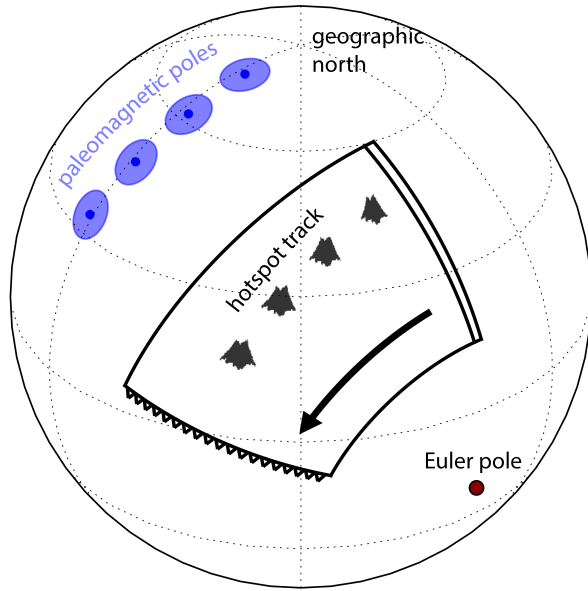


**Figure 1.** Conceptual model for a paleomagnetic Euler pole. A finite rotation of a plate around an Euler pole (dark red circle) results in arcuate oceanic fracture zones and hotspot tracks (cartoon mountain) which describe small circles on the globe. The same finite rotation produces a circle in the APWP, which is illustrated by blue paleomagnetic poles. By fitting a small/great circle to the APWP, we may recover the Euler pole that produced the rotation which is termed the paleomagnetic Euler pole. Cartoon is adapted from Gordon et al. (1984).

71 inversions are not a single answer, but are instead a distribution of possible answers, furnishing  
 72 uncertainties as part of the solution process. Proper treatment of uncertainties also allow  
 73 researchers to avoid overfitting models to noise. For instance, Iaffaldano et al. (2012) employed a  
 74 similar Bayesian approach to inversions for finite plate rotations. They used seafloor data to  
 75 reconstruct India's Cenozoic convergence with Asia, incorporating uncertainties into the inversion.  
 76 In the process, they demonstrated that interpretations of changes in plate motions on timescales  
 77 <1 Myr are the result of overfitting of data and there are fewer kinematic changes and longer  
 78 stability in plate motions than suggested by some previous treatments.

79 In the sections below, we first review different approaches that have been applied to synthesize  
 80 and interpret APWPs. We then describe the formalism of Bayesian inversions and Markov chain  
 81 Monte Carlo methods that we will apply. We then describe the statistical model which we will be  
 82 inverting and demonstrate the inversion of several synthetic data sets. Finally, we show case  
 83 studies where we apply the method to paleomagnetic poles in order to develop estimates of  
 84 paleomagnetic Euler pole positions and obtain estimates of plate velocity.

## 85 Interpretation of apparent polar wander paths

86 A sequence of paleomagnetic poles from the same continental block can be synthesized into an  
 87 APWP, which can then be used to develop plate tectonic reconstructions and models of plate  
 88 motion through time. Interpretation of these paths becomes difficult in the case of limited,  
 89 uncertain, or conflicting data, and when the age of paleomagnetic poles are poorly known. A  
 90 number of approaches to dealing with uncertainties in APWPs have been developed, which we  
 91 briefly review here.

92 **Latitudinal drift**

93 A paleomagnetic pole provides constraints on the paleolatitude and orientation of a lithospheric  
94 block. However, due to the rotational symmetry of Earth's time-averaged geocentric axial dipole  
95 magnetic field, paleomagnetic poles do not directly constrain absolute paleolongitude (Butler,  
96 1992). The simplest analysis of an APWP is to compare the paleolatitudes implied by successive  
97 poles for a point on a respective block. The difference in paleolatitudes gives a minimum angular  
98 distance over which the block has traveled. When this distance is compared to the age difference  
99 between the poles, such a comparison establishes a rate of latitudinal motion.

100 It is possible to estimate confidence bounds on the rate of latitudinal drift through bootstrap  
101 resampling (e.g. Tarduno et al., 1990) or by taking a Monte Carlo approach. Swanson-Hysell  
102 et al. (2014) developed a Monte Carlo sampling method and applied the method to a pair of poles  
103 from the Proterozoic Midcontinent Rift of North America to estimate the range of implied  
104 latitudinal drift. They also sampled from the uncertainties of radiometric dates associated with  
105 the poles, assuming Gaussian distributions, in order to incorporate age uncertainties into the  
106 analysis. With samples of pole position and ages, they were able to estimate the 95% confidence  
107 estimates on the rate of latitudinal drift.

108 Whether using point estimates of the latitudinal drift rate or using Monte Carlo estimates, the  
109 latitudinal drift interpretation of APWPs remains limited as it represents a minimum estimate of  
110 total plate motion. It does not resolve longitudinal drift rate, nor does it naturally extend to  
111 APWPs with more than two poles, especially if two coeval poles are not in agreement, as it  
112 requires the selection of pole pairs.

113 **Spherical splines**

114 When considering APWPs with many poles, it becomes more difficult to perform latitudinal  
115 comparisons between pairs of poles. It is not always clear which pairs of poles to compare in cases  
116 where there are many overlapping paleomagnetic poles that have variable uncertainties associated  
117 with their positions and ages.

118 One approach to synthesize such data is to fit a spline through the set of paleomagnetic poles,  
119 constraining the path to lie on the surface of a sphere. This approach was pioneered by Torsvik  
120 et al. (1992) using the spherical spline algorithm developed by Jupp and Kent (1987). This  
121 approach has the advantage of allowing the paleomagnetic pole data to be weighted by their  
122 spatial uncertainties. The uncertainty assigned to a paleomagnetic pole can be the 95%  
123 confidence interval on the pole position, but it can also be augmented by various quality screening  
124 factors, such as the quality ("Q") factor of Van der Voo (1990) (Torsvik et al., 1992). Even with  
125 the weighting of the paleomagnetic poles by uncertainty, there can be unrealistic loops in the  
126 APWP generated by the spline fit. To combat this behavior, the spline can also be computed  
127 under tension which penalizes curvature and produces a smoother path (Torsvik et al., 1996).

128 The spherical spline approach to interpreting APWPs has attractive features. It produces a  
129 smooth path through the data that can incorporate spatial uncertainties in the data, and may be

130 efficiently computed. However, it does have some drawbacks. It is not easy to determine the  
131 appropriate uncertainty weighting and spline tension parameters for the fit, and what effect those  
132 choices have on the result. Furthermore, the resulting fit does not have an uncertainty with a  
133 physically interpretable meaning (Torsvik et al., 1996). It also does not have a simple way of  
134 incorporating age uncertainties of the paleomagnetic poles. Finally, by their nature, splines do  
135 not readily represent the sharp hairpin cusps that characterize abrupt shifts in motion that plates  
136 sometimes undergo (Irving and Park, 1972; Gordon et al., 1984).

137 **Running means**

138 An alternative method for developing APWPs is to perform a running Fisher mean on the poles  
139 with a moving window (Irving, 1977; Van der Voo and Torsvik, 2001; Torsvik et al., 2008). In  
140 such an analysis, paleomagnetic poles in a compilation are averaged with a defined window  
141 duration (typically 10-30 Myr) with the duration of the moving window controlling the amount of  
142 smoothing. Like spherical splines, the running mean approach has the ability to effectively damp  
143 the effect of outlier poles that could lead to spurious motion in the APWP if there are sufficient  
144 data. Furthermore, this moving window method enforces an age progression in the averaged  
145 poles. Torsvik et al. (2008) also investigated the effects of combining running means with  
146 spherical splines, by first computing a set of mean poles and then fitting a spline through those  
147 means. The simplicity of using the running mean approach to develop an APWP, as well as its  
148 ability to suppress potentially spurious poles, has led to it being widely adopted.

149 The running mean approach shares many of the drawbacks of the spline approach. It is not  
150 obvious how to best choose the window duration, and different window durations are likely  
151 appropriate for different data sets. It is also unclear how to interpret the resulting uncertainties in  
152 the path that are reported as the Fisher A<sub>95</sub> ellipse of the mean of the poles. This approach,  
153 along with the spherical spline method, does not easily incorporate age uncertainties in the poles,  
154 nor the uncertainty in pole positions.

155 **Paleomagnetic Euler poles**

156 The idea of fitting small circles to paleomagnetic data to gain insight into plate motions was first  
157 described by Francheteau and Sclater (1969). The center of such a circle on a sphere is the pole of  
158 rotation which was termed a paleomagnetic euler pole by Gordon et al. (1984) who developed a  
159 method to invert for the position of such poles. The approach builds on the recognition that plate  
160 motions are well described by finite rotations around Euler poles which are approximately steady  
161 for millions or tens of millions of years. As a result, the APWP of a plate can be described by  
162 Euler rotations, which produce small circle paths on Earth's surface (Fig. 1). Therefore,  
163 paleomagnetic Euler pole analysis conforms to the general model of the movement of tectonic  
164 plates. Since the analysis solves for the Euler pole that produces a given small circle, this  
165 approach allows for an estimate of the full motion of a given plate, including the total plate speed  
166 (instead of just the latitudinal component of the speed). Effectively, the analysis utilizes both the  
167 change in plate orientation and latitude information embedded within paleomagnetic poles to

<sup>168</sup> estimate both latitudinal and longitudinal motion as succinctly specified by Euler pole  
<sup>169</sup> parameters.

<sup>170</sup> However, paleomagnetic Euler pole analysis has many of the same deficiencies that spline fits  
<sup>171</sup> and running means have—it is not easy to compute uncertainties, especially in the presence of  
<sup>172</sup> unknown ages of poles. Furthermore, one has the additional challenge and related uncertainty of  
<sup>173</sup> deciding how many paleomagnetic Euler poles to include for a given sequence of paleomagnetic  
<sup>174</sup> poles. In this contribution, we develop a Bayesian statistical approach to paleomagnetic Euler  
<sup>175</sup> pole analysis which attempts to address some of these deficiencies.

## <sup>176</sup> Bayesian inversion

### <sup>177</sup> A general description of inverse problems

<sup>178</sup> The central question motivating inverse problems is “How probable is a particular model, given  
<sup>179</sup> my observations?”. We represent a vector of individual observations by the data vector  $\mathbf{d}$ , and a  
<sup>180</sup> model by the vector of model parameters  $\mathbf{m}$ , so the above question can be expressed as the  
<sup>181</sup> function  $P(\mathbf{m}|\mathbf{d})$ . Traditional frequentist approaches to an inverse problem often proceed by  
<sup>182</sup> maximizing the likelihood function, defined by the probability of the data given a particular  
<sup>183</sup> model (e.g Aster et al., 2005):

$$\mathcal{L}(\mathbf{m}|\mathbf{d}) \equiv P(\mathbf{d}|\mathbf{m}). \quad (1)$$

<sup>184</sup> The likelihood function replaces something that is difficult to compute (namely,  $P(\mathbf{m}|\mathbf{d})$ ) with  
<sup>185</sup> something that is less difficult to compute. To compute  $\mathcal{L}(\mathbf{m}, \mathbf{d})$  we need to have two things: a  
<sup>186</sup> statistical model for uncertainties in the observations  $\mathbf{d}$  and a forward model that allows us to  
<sup>187</sup> compute predictions. We denote the forward model by  $\mathbf{g}$ :

$$\mathbf{d}^p = \mathbf{g}(\mathbf{m}), \quad (2)$$

<sup>188</sup> where the superscript “ $p$ ” denotes a predicted value. If each of the observed data  $d_i$  are described  
<sup>189</sup> by Gaussian random variables with standard deviations  $\sigma_i$ , the likelihood function is given by the  
<sup>190</sup> product of the individual likelihoods of the observations:

$$\mathcal{L}(\mathbf{d}|\mathbf{m}) = \prod_i \exp\left(-\frac{(d_i - d_i^p)^2}{2\sigma_i^2}\right). \quad (3)$$

<sup>191</sup> The likelihood function  $\mathcal{L}$  is maximized by searching over the model parameter space. If the  
<sup>192</sup> uncertainties in the observations are Gaussian, then maximizing the likelihood function is  
<sup>193</sup> equivalent to the least squares solution (Aster et al., 2005).

<sup>194</sup> A standard maximum likelihood fit will frequently overfit the observations, resulting in  
<sup>195</sup> unrealistic solutions. In the context of APWPs, these overfit solutions may pass through every  
<sup>196</sup> paleomagnetic pole, including less reliable ones, resulting in loopy or jerky paths. In order to  
<sup>197</sup> address such overfitting, some form of regularization is usually included in the solution of the  
<sup>198</sup> inverse problem, such as penalizing the magnitude or curvature of the solution. Both the

199 running-mean and the spline under tension approaches to APWPs are a form of regularization on  
 200 the problem.

201 **Bayesian approach**

202 The Bayesian approach to inverse problems takes a different strategy from the frequentist one.  
 203 Rather than finding point estimates of a model fit, it treats the underlying model as a set of  
 204 random variables with individual probability distributions. The probability distribution of the  
 205 model given the data ( $P(\mathbf{m}|\mathbf{d})$ ) is then found by an application of Bayes theorem (cf. Sivia and  
 206 Skilling, 2006):

$$P(\mathbf{m}|\mathbf{d}) = \frac{P(\mathbf{d}|\mathbf{m}) P(\mathbf{m})}{P(\mathbf{d})}. \quad (4)$$

207 It is often unnecessary to calculate the denominator of Equation (4), which is a normalization  
 208 constant, leaving us with

$$P(\mathbf{m}|\mathbf{d}) \propto P(\mathbf{d}|\mathbf{m}) P(\mathbf{m}). \quad (5)$$

209 The quantity  $P(\mathbf{m}|\mathbf{d})$  is known as the posterior probability, and it represents our desired  
 210 knowledge about the distributions of the parameters  $\mathbf{m}$ . The first factor on the right-hand-side of  
 211 Equation (5) is identical to the likelihood function described above, and the second factor is  
 212 known as the prior probability of the model.

213 The prior probability reflects the state of our knowledge and beliefs of the values of the model  
 214 parameters prior to the consideration of our data. It also allows us to incorporate theoretically or  
 215 empirically derived constraints that are not otherwise included in the forward model. In contrast  
 216 with the classical statistical approach of regularization, the Bayesian inverse problem can (in  
 217 effect) regularize the problem by making choices of probability distributions that have less  
 218 probability density in regions with less realistic values (e.g. Minson et al., 2013; Sambridge et al.,  
 219 2013).

220 **Markov chain Monte Carlo methods**

221 It is usually impossible to calculate the posterior probability distribution in Equation (4) directly  
 222 (Davidson-Pilon, 2015). It is much more tractable to generate a Markov chain which, upon  
 223 convergence, generates samples from the desired posterior (Gelman et al., 2013). This approach  
 224 defines a class of methods known as Markov chain Monte Carlo (MCMC) methods.

225 The literature on MCMC methods is extensive and we do not review it here, but references the  
 226 interested reader could refer to for further introduction include Gelman and Rubin (1996),  
 227 Sambridge et al. (2013), and Davidson-Pilon (2015). A number of high-quality open source  
 228 software packages for implementing MCMC models exist, including WinBUGS (Lunn et al.,  
 229 2000), PyMC3 (Salvatier et al., 2016), and Stan (Carpenter et al., 2017). We make extensive use  
 230 of PyMC3 in this work.

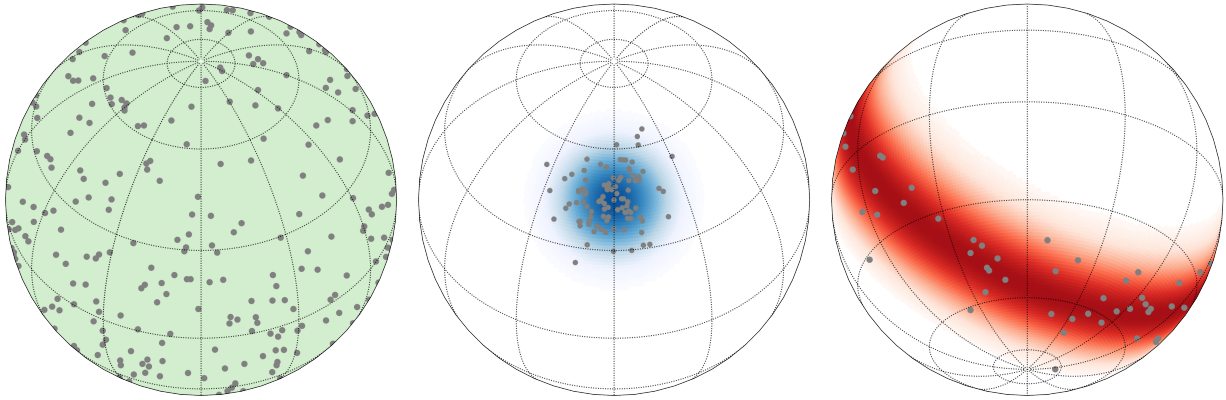


**Figure 2.** Probability densities for distributions of directional data, as well as samples drawn from them. All distributions are plotted using an orthographic projection. (left panel) Uniform distribution. (middle panel) Fisher distribution. The center of the distribution is at 45°N, 30°E, with concentration parameter of  $\kappa = 50$ . (right panel) Watson girdle distribution. The pole of symmetry is at 30°N, 30°E, with a concentration parameter of  $\kappa = -25$ .

### 231 Distributions on a sphere

232 In order to proceed with a Bayesian description of the problem, every parameter in the model  
 233 needs to be described by some statistical distribution that determines the probability that the  
 234 parameter takes a specific value. Parameters like pole ages can be described by 1D probability  
 235 distributions (such as uniform or normal distributions), whereas Euler pole locations are  
 236 described by 2D distributions of directional data on the surface of a sphere. We review several of  
 237 these distributions here. For a comprehensive discussion of spherical probability distributions, see  
 238 Fisher et al. (1987). Plots of the following distributions (uniform, Fisher, and Watson), as well as  
 239 samples drawn from them, are shown in Figure 2.

### 240 Uniform distribution

241 The simplest probability distribution on a sphere is the spherical uniform distribution. It has a  
 242 probability density given by

$$\rho_U(\phi, \psi) = \frac{1}{4\pi}, \quad (6)$$

243 where  $\rho_U$  is the probability density,  $\phi$  is the longitude, and  $\psi$  is the latitude (we will also refer to  
 244 the Cartesian unit vector  $\hat{\mathbf{x}}$  as a concise representation of  $\phi$  and  $\psi$ ). Non-uniform distributions on  
 245 a sphere reduce to the uniform distribution in some limit (i.e. the Fisher distribution as the  
 246 precision parameter goes to zero). We use the uniform distribution when we want to specify an  
 247 uninformative prior distribution for directional parameters.

<sup>248</sup> **Fisher distribution**

<sup>249</sup> The Fisher distribution (also called the von Mises-Fisher distribution) is the analogue of a 2D  
<sup>250</sup> normal distribution on a sphere (Fig. 2). The probability density  $\rho_F$  at a point  $\hat{\mathbf{x}}$  is given by

$$\begin{aligned}\rho_F(\phi, \psi; \kappa_F, \hat{\boldsymbol{\mu}}) &= \frac{1}{C_F} \exp(\kappa_F \hat{\mathbf{x}}^T \hat{\boldsymbol{\mu}}) \\ &= \frac{1}{C_F} \exp(\kappa_F \cos \theta),\end{aligned}\tag{7}$$

<sup>251</sup> where  $\kappa_F$  is the concentration of the distribution,  $\hat{\boldsymbol{\mu}}$  the unit vector for the mean direction of the  
<sup>252</sup> distribution, and  $C_F$  is a normalization coefficient. It can be alternatively parameterized using  $\theta$ ,  
<sup>253</sup> which is the angle between  $\hat{\mathbf{x}}$  and  $\hat{\boldsymbol{\mu}}$ . The normalization factor is given by

$$C_F = \frac{\kappa_F}{4\pi \sinh \kappa_F}.\tag{8}$$

<sup>254</sup> When  $\kappa_F$  goes to zero, the Fisher distribution is equivalent to the spherical uniform distribution.

<sup>255</sup> The uncertainty ellipses for paleomagnetic poles are typically calculated assuming a Fisher  
<sup>256</sup> distribution of the underlying data, and we will use this distribution to calculate the likelihood  
<sup>257</sup> function for pole positions in the model.

<sup>258</sup> **Watson girdle distribution**

<sup>259</sup> Whereas the Fisher distribution concentrates probability density around a pole on the surface of  
<sup>260</sup> the sphere, the Watson girdle probability distribution is concentrated in a belt orthogonal to the  
<sup>261</sup> pole (Fig. 2). It is useful for characterizing planar data, and is given by

$$\begin{aligned}\rho_W(\phi, \psi; \kappa_W, \hat{\boldsymbol{\mu}}) &= \frac{1}{C_W} \exp(\kappa_W (\hat{\mathbf{x}}^T \hat{\boldsymbol{\mu}})^2) \\ &= \frac{1}{C_W} \exp(\kappa_W \cos^2 \theta),\end{aligned}\tag{9}$$

<sup>262</sup> where  $\kappa_W$  is the concentration of the girdle,  $C_W$  is a normalization coefficient, and the other  
<sup>263</sup> parameters are identical to those in the Fisher distribution. The Watson distribution is  
<sup>264</sup> girdle-shaped only when  $\kappa_W$  is a negative number, which is the only case we consider here.

<sup>265</sup> The normalization factor is given by

$$C_W = \left[ {}_1F_1\left(\frac{1}{2}, \frac{3}{2}, \kappa_W\right) \right]^{-1},\tag{10}$$

<sup>266</sup> where  ${}_1F_1()$  is Kummer's confluent hypergeometric function, which is available in most software  
<sup>267</sup> libraries of special mathematical functions. As with the Fisher distribution, when  $\kappa_W$  goes to  
<sup>268</sup> zero, the Watson distribution is equivalent to the spherical uniform distribution.

---

## 269 A model for paleomagnetic Euler pole inversion

### 270 Forward model

271 A forward model describes how we generate predicted observations given a set of model  
 272 parameters (Equation (2)). The forward model for paleomagnetic Euler pole analysis in this  
 273 study is essentially unchanged from that of Gordon et al. (1984). We describe plate motions (and  
 274 hence paleomagnetic pole motions) with a series of Euler poles. Each Euler pole has three  
 275 parameters: a latitude, a longitude, and a rotation rate.

276 In a model with multiple Euler poles, we also must specify the ages where one Euler pole  
 277 switches to the next (the cusps, or “hairpins” of Irving and Park (1972)). In the context of  
 278 parameter inversion, these ages are often known as “changepoints.”

279 Finally, we need a starting position on the globe, which, in practice, can be sampled from the  
 280 Fisher distribution of the oldest paleomagnetic pole in the data set. The starting point  
 281 contributes two parameters (a latitude and a longitude).

282 Therefore, a model with  $n_e$  Euler rotations will have  $3n_e$  parameters for the poles,  $(n_e - 1)$   
 283 parameters for the changepoints, and 2 parameters for the starting location. The number  
 284 parameters for which we are inverting is then given by

$$\begin{aligned} N &= 3n_e + (n_e - 1) + 2 \\ &= 4n_e + 1. \end{aligned} \tag{11}$$

285 For each Euler pole,  $\omega_i$  the velocity  $\mathbf{v}$  of a point  $\mathbf{p}$  on the surface of the globe is given by

$$\mathbf{v} = \omega_i \times \mathbf{p}. \tag{12}$$

286 Finite rotations can be performed by constructing Euler angle rotation matrices (cf. Goldstein,  
 287 1965). We generate synthetic paleomagnetic pole positions from the forward model by stringing  
 288 together finite rotations through the stage poles until the age of the paleomagnetic pole is reached.  
 289 These positions can then be compared to the actual paleomagnetic poles in a given dataset.

### 290 Choice of prior distributions

291 Bayesian analysis requires us to specify prior probability distributions for each of the model  
 292 parameters in the inverse problem. These distributions reflect our state of knowledge about the  
 293 values of the parameters before we begin, and allow us the option of incorporating information  
 294 otherwise not captured by the model. To avoid biasing the results of the model towards a specific  
 295 posterior distribution, we usually try to choose prior distributions that are as uninformative as  
 296 possible. Depending upon the context, and the type of parameter, that choice may vary. The  
 297 central parameters in the paleomagnetic Euler pole problem are the Euler pole positions, the  
 298 Euler pole magnitudes, the changepoints, the starting point, and the paleomagnetic pole ages,

299 which we treat in turn. We use the notation  $x \sim y$  to indicate that the parameter  $x$  is drawn from  
300 distribution  $y$ .

301 **Euler pole directions:** The first parameter we consider is the position of the Euler poles,  
302 which should be drawn from a spherical probability distribution. The least informative prior  
303 distribution for the i'th Euler pole is the uniform spherical distribution:

$$\hat{\omega}_i \sim \rho_U. \quad (13)$$

304 essentially allowing the Euler pole to be anywhere on the globe with equal probability.

305 An alternative choice is to inform our prior distribution for Euler pole positions based on  
306 observation of modern plate motions. It has long been observed that, to first order, plate motions  
307 are well explained by slab-pull torques acting along subduction zones, and to a lesser extent, ridge  
308 push and mantle traction effects (Forsyth and Uyeda, 1975; Gordon et al., 1978; Richardson,  
309 1992).

310 We can ask the question of whether the Euler pole for a given plate is more likely to be on top  
311 of the plate (corresponding to a spinning motion for that plate) or away from that plate  
312 (corresponding to motion across the surface of Earth). Given that tectonic plates can broadly be  
313 considered to be the surface expression of mantle convection, we can hypothesize that the second  
314 possibility is more likely because a spinning plate has no divergence (i.e., spreading centers and  
315 subduction zones, (Forte and Peltier, 1987; Gable et al., 1991)). Without divergence, the plate  
316 motion does not contribute to large-scale convection.

317 To evaluate this hypothesis, we generated position samples on the surface of Earth and  
318 computed the angular distance between that point and the Euler pole for the plate in which that  
319 point resides. We used the NNR-MORVEL56 model for current plate motions (Argus et al., 2011)  
320 and restricted our analysis to the fourteen largest plates. We then fit those angular distance  
321 samples to a Watson girdle distribution (Equation (9)), inverting for the concentration parameter  
322  $\kappa_W$ . If an Euler pole position has no preference for being a particular angular distance from a  
323 point on a plate, then  $\kappa_W$  should be close to zero, corresponding to a uniform distribution. We  
324 find that the distribution is best fit with  $\kappa_W \approx -0.8$ , which corresponds to the Euler pole  
325 probability density being roughly twice as large  $90^\circ$  away from a given point than on top of the  
326 point (Fig. 3).

327 **Euler pole magnitudes:** The magnitude of each Euler pole is a positive number, specifying  
328 the rotation rate of that pole (negative rotations can be accommodated by flipping an Euler pole  
329 to the antipode). There are several possibilities for the prior distribution for the rates. In order to  
330 not bias the inversion towards a particular rate, we can choose a uniform prior distribution with  
331 large support:

$$|\omega_i| \sim U(0, 4), \quad (14)$$

332 where  $U(\cdot, \cdot)$  is a uniform distribution between two values, and is specified in degrees per million  
333 years. Typical rotation rates for present day plate motions are under  $1^\circ/\text{Myr}$  (Argus et al., 2011),  
334 which corresponds to plate speeds of about 11 cm/yr at a position  $90^\circ$  from the Euler pole.

335 Another option is to choose a weakly informative prior distribution for the Euler pole  
336 magnitudes informed by recent plate motions (similar our approach of the Watson girdle prior

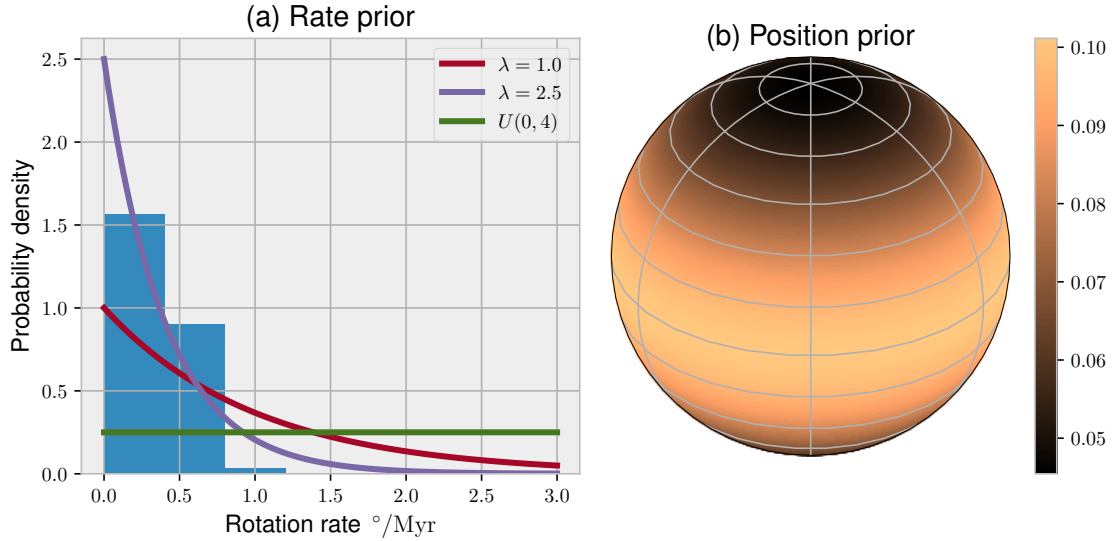


**Figure 3.** Informative prior distributions for Euler poles. (a) Prior probabilities for rotation rates. The histogram is the angular rotation rate from one thousand samples from the surface of Earth, using the NNR-MORVEL56 model. A fit to this sample set with an exponential distribution yields a scale parameter of  $\lambda \approx 2.5$ . We also show the distribution for  $\lambda = 1.0$ , which imposes less regularization on the rate as a less restrictive prior distribution, and a uniform  $U(0, 4)$  distribution between 0 and  $4^\circ/\text{Myr}$ , which specifies no preference for slower speeds if set as the prior probability. (b) Prior probability density for the position of the Euler poles, with the north pole as the site latitude and longitude. We again sampled one thousand points on Earth's surface, calculating the angular distance between that point and the Euler pole for its plate. If we model the probability distribution as being drawn from a Watson distribution, these angular distances correspond to colatitudes, where the pole is the sampled point. Fitting the resulting angular distribution to a Watson girdle distribution finds  $\kappa_W \approx -0.8$ . Since the Watson distribution is rotationally symmetric, longitudes do not contribute to the fit. For  $\kappa_W \approx -0.8$  the probability density is roughly twice as large at the equator ( $90^\circ$  from a plate) as at the pole (on top of the plate).

337 distribution for Euler pole position). Zahirovic et al. (2015) found, based on analysis of Cenozoic  
 338 and Mesozoic plate reconstructions, that plate speeds much higher than 15 cm/yr were unlikely to  
 339 be sustained. A reasonable choice of distribution for strictly positive numbers is the exponential  
 340 distribution, given by

$$\rho_E(|\omega_i|) = \lambda \exp(-\lambda|\omega_i|), \quad (15)$$

341 which has higher probability density at lower values, and falls off exponentially toward higher  
 342 values. We sampled the current plate rates on Earth's surface according to NNR-MORVEL56 and  
 343 fit those to an exponential distribution. The best fitting scale parameter  $\lambda$  for current plate rates  
 344 is  $\sim 2.5$  (Fig. 3). Making this choice of prior distribution for Euler pole rotation rates can be seen  
 345 as a form of regularization on plate speeds. A scale parameter of 1 (also shown in Fig. 3) could  
 346 reflect similar knowledge about the distribution of plate speeds with a less restrictive  
 347 regularization.

348 **Changepoints:** Changepoints occur sequentially between the oldest (at age  $a_{\max}$ ) and  
 349 youngest (at age  $a_{\min}$ ) paleomagnetic poles. We choose a uniform distribution as a prior for these

350 changepoints:

$$c_i \sim U(a_{\min}, a_{\max}), \quad (16)$$

351 where  $c_i$  is the i'th changepoint.

352 **Starting position:** Finally, the starting position  $\hat{\mathbf{x}}_{\text{start}}$  for the set of Euler pole rotations  
 353 needs a prior distribution. We could choose another uniform distribution, but a more reasonable  
 354 choice is to start near the oldest paleomagnetic pole in the dataset. We therefore choose the Fisher  
 355 distribution of the oldest paleomagnetic pole as a reasonable prior distribution for a start point:

$$\hat{\mathbf{x}}_{\text{start}} \sim \rho_F(\kappa_{F0}, \hat{\boldsymbol{\mu}}_0), \quad (17)$$

356 where  $\kappa_{F0}$  and  $\hat{\boldsymbol{\mu}}_0$  are the concentration parameter and mean direction of the oldest  
 357 paleomagnetic pole in the dataset.

358 **Pole ages:** One of the major advantages of Bayesian analysis is the ability to naturally  
 359 incorporate uncertainties in as many parameters as needed. Previous approaches to modeling  
 360 APWPs have the drawback that they do not easily account for uncertainties in the age of  
 361 paleomagnetic poles. In our approach, we can include age uncertainty by including the age of the  
 362 poles and associated uncertainty as parameters in our model.

363 There are many different ways to constrain the ages of the geologic units from which we obtain  
 364 paleomagnetic poles, including radiometric dating, biostratigraphy, magnetostratigraphy, and  
 365 cross-cutting relationships. Here we concentrate on poles that are either interpreted to be the age  
 366 of a single radiometric date or are interpreted to be bracketed stratigraphically between two dates  
 367 (derived radiometrically or by using other age control such as biostratigraphy). If a geologic unit  
 368 has been radiometrically dated, we can model the age of the j'th paleomagnetic pole  $a_j$  as a  
 369 normal distribution with mean  $\mu_j$  and standard deviation  $\sigma_j$ :

$$a_j \sim N(\mu_j, \sigma_j), \quad (18)$$

370 where  $N(.,.)$  denotes a normal distribution.

371 Frequently, however, the geologic unit from which we obtain a paleomagnetic pole is not well  
 372 dated, but its age can be constrained to lie between those of well-dated units stratigraphically  
 373 above and below it, dates obtained by cross-cutting relationships, or a number of dated units  
 374 within a broader province. In these cases, a uniform distribution between those ages is a  
 375 reasonable choice for the prior distribution:

$$a_j \sim U(a_{\text{young}}, a_{\text{old}}), \quad (19)$$

376 where  $a_{\text{young}}$  and  $a_{\text{old}}$  are the ages of the lower and upper age constraints, respectively.

377 To summarize our choices for prior distributions:

- 378 • Euler pole positions: spherical uniform distribution, or a Watson girdle distribution with  
 379  $\kappa_W \approx -0.8$ .
- 380 • Euler pole magnitudes: Uniform distribution between  $0^\circ$  and  $4^\circ/\text{Myr}$ , or an exponential  
 381 distribution with  $\lambda \approx 2.5$  or  $\lambda \approx 1$ .

- Changepoints: uniform distribution between  $a_{\min}$  and  $a_{\max}$ .
- Paleomagnetic pole ages: normal or uniform distribution, depending on the type of age control for the geologic unit from which the pole was obtained.

## 385 Likelihood

386 In addition to the choice of prior distributions, we need a statistical description of the  
 387 observations. This description will allow us to calculate the likelihood function, which, when  
 388 combined with the prior distributions, allows us to evaluate Bayes' theorem (Equation (5)).

389 In the case of APWPs, our observations are paleomagnetic poles. The most common statistical  
 390 distribution for describing paleomagnetic poles is the Fisher distribution (although other  
 391 distributions are sometimes used, such as the Kent or Bingham distributions, c.f. Tauxe, 2010).  
 392 Given the set of model parameters  $\mathbf{m}$  and the forward model  $\mathbf{g}(\mathbf{m})$ , described above, we can  
 393 calculate the predicted paleomagnetic pole unit vectors  $\hat{\mathbf{x}}_i^p$ . For a set of  $n$  paleomagnetic poles,  
 394 the likelihood is then given by the product of the probabilities of each observation of  
 395 paleomagnetic pole position and age:

$$P(\mathbf{d}|\mathbf{m}) = \prod_{i=1}^n \frac{1}{C_{F,i}} \exp \left( \kappa_{F,i} \hat{\mathbf{x}}_i^{pT} \hat{\boldsymbol{\mu}}_i \right) \cdot a_i. \quad (20)$$

## 396 Example inversions

397 Before proceeding with inversions for paleomagnetic Euler poles using real paleomagnetic data, it  
 398 is useful to consider a few examples of inversions for synthetic datasets. We have specified the  
 399 forward model described above using the package PyMC3 (Salvatier et al., 2016) which enables us  
 400 to perform the inversion. Within PyMC3, we are able to specify custom probability distributions  
 401 enabling the directional data distributions illustrated in Figure 2 to be implemented. The Markov  
 402 chain Monte Carlo (MCMC) analysis uses the Metropolis–Hastings algorithm for sampling. Our  
 403 code for the inversions has an open-source GPL license and is available on Github  
 404 [https://github.com/Swanson-Hysell-Group/Bayesian\\_PEP\\_inversion](https://github.com/Swanson-Hysell-Group/Bayesian_PEP_inversion) and archived on Zenodo (*we  
 405 will archive the Github repository on Zenodo at the time of proofs following any revisions which  
 406 provides long-term assurance of archival and will add the link here*).

## 407 One Euler rotation

408 We begin by trying to recover the Euler pole for a single rotation. We generate an idealized  
 409 synthetic APWP of four poles by starting from a pole at 19° N, 024° E, and rotating around an  
 410 Euler pole at 00° N, 000° E for 100 Myr at a rate of 1°/Myr. We produce paleomagnetic poles at  
 411 100 Ma, 75 Ma, 50 Ma, and 25 Ma, and prescribe A<sub>95</sub> of 4° to each pole (where A<sub>95</sub> indicates the  
 412 95% angular confidence for the pole position).

413 The results of the inversion are shown in Figure 4. The Bayesian approach successfully  
414 recovers a posterior probability distribution for the position of the Euler pole that includes the  
415 start pole, as well as a rate that is centered near the true value of  $1^\circ/\text{Myr}$  (Fig. 4). The posterior  
416 distribution for the rate has a highest posterior density scredible interval at 95% (which we  
417 abbreviate from here as a 95% credible interval) between  $0.7^\circ/\text{Myr}$  and  $1.2^\circ/\text{Myr}$ , reflecting the  
418 resolving power of the inversion for data with the given uncertainties.

#### 419 Two Euler rotations

420 We next consider an inversion for an APWP with two stage poles. Unlike the previous example  
421 where we inverted for a single Euler pole, this inversion also requires a changepoint. We generate  
422 nine idealized paleomagnetic poles with  $A_{95}$  of  $4^\circ$  for each from a starting point at  $5^\circ\text{S}$ ,  $030^\circ\text{E}$ .  
423 The first rotation is around an Euler pole at  $10^\circ\text{S}$ ,  $000^\circ\text{E}$ , and rotates at  $1.5^\circ/\text{Myr}$  for 60 Myr.  
424 The second rotation is around an Euler pole at  $10^\circ\text{N}$ ,  $300^\circ\text{E}$  and rotates at a rate of  $0.75^\circ/\text{Myr}$   
425 for the same amount of time. The synthetic poles associated with this two stage model are shown  
426 in Figure 4.

427 The inversion successfully recovers the Euler pole rotation rates with posterior distributions  
428 centered near the true values. The inversion also successfully recovers the changepoint of 60 Ma  
429 between the first and second Euler pole with a 95% credible interval for the changepoint of 65 to  
430 55 Ma. The inverted Euler pole positions for the first stage pole (Fig. 4 blue distributions) are  
431 centered near the true location (Fig. 4 blue star) and the inverted second Euler pole positions  
432 (Fig. 4 red distributions) encompass the true location as well (Fig. 4 red star). There is a larger  
433 spread in credible Euler pole positions for the second Euler pole particularly in the direction  
434 perpendicular to the APWP. The greater uncertainty on the location of the second Euler pole  
435 results from the motion along the APWP being smaller relative to the uncertainty on the  
436 paleomagnetic pole positions. As a result, the inverted paths have more variable curvature.

437 Overall, this example demonstrates that the inversion framework can resolve APWPs with  
438 more than one stage pole and provides posterior probability distributions on the Euler rotation  
439 changepoint in addition to the multiple Euler poles positions and rates (Fig. 4).

#### 440 Incorporating age uncertainty

441 A benefit of the Bayesian approach to inverse problems is its generality. As long as some effect  
442 can be described statistically and incorporated into our forward model, we can include it in the  
443 inverse problem. As a result, we are able to include uncertainties on the ages of paleomagnetic  
444 poles. We use a similar test case as in the one Euler pole inversion with the ages of synthetic  
445 poles being adjusted to span from 140 Ma to 40 Ma (poles of 140, 115, 90, 65, and 40 Ma) (Fig.  
446 5A), but assign prior distributions for the ages of the poles. For the first and last poles, we  
447 assume they are radiometrically dated with standard deviations of 5 Myr. However, we assume  
448 that the middle three poles have no age control, except that their ages are constrained to be  
449 between the first and last poles. We thus assign Gaussian prior distributions to the first and last

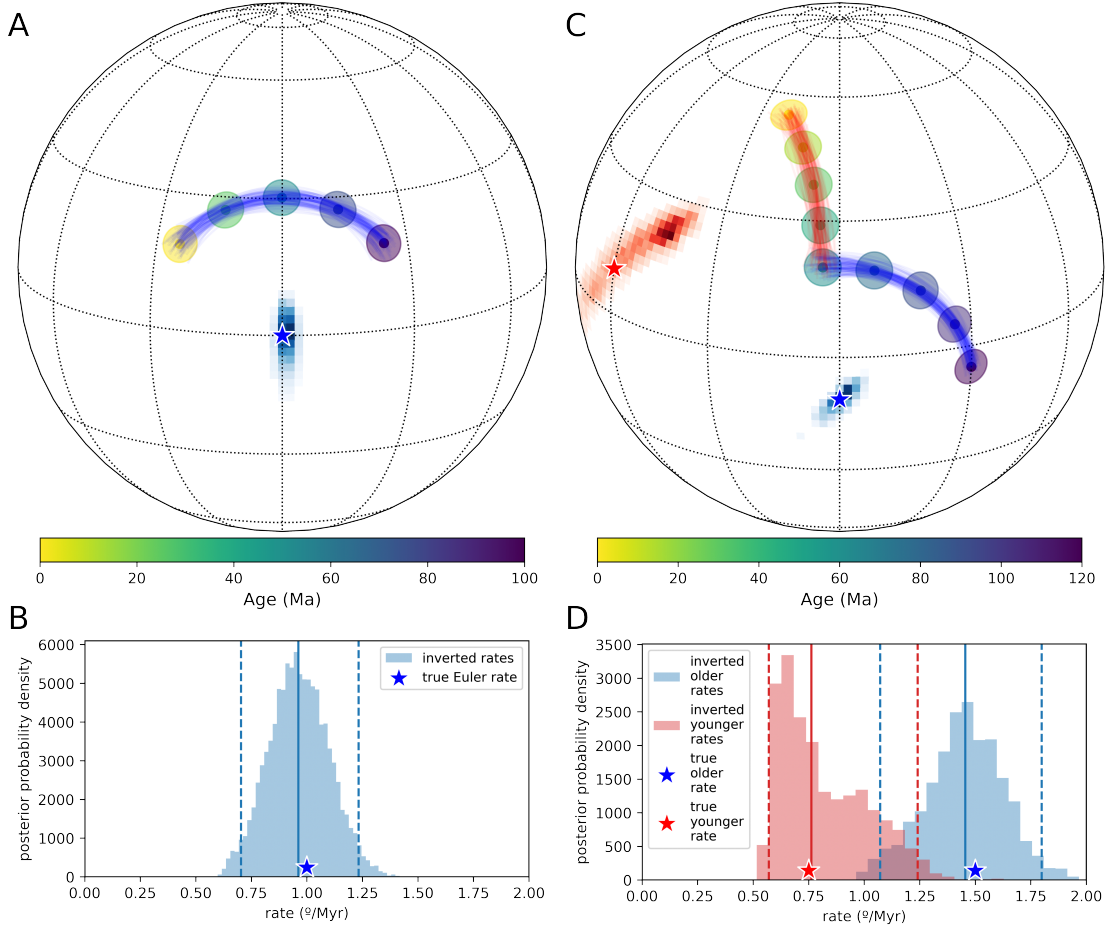


**Figure 4.** Inversion for Euler poles from synthetic data. (A) Five paleomagnetic poles are generated during a net  $100^{\circ}$  rotation about an Euler pole at  $00^{\circ}\text{N}$ ,  $000^{\circ}\text{E}$  over 100 Myr, for a rotation rate of  $1^{\circ}/\text{Myr}$ . The blue distribution is the probability density of Euler pole positions recovered by MCMC inversion, and the blue arcs are 100 of the resulting synthetic APWPs (sampled from 50,000). (B) Posterior probability density for the rotation rate of the Euler pole recovered by the inversion. The solid line shows the median of the distribution ( $0.96^{\circ}/\text{Myr}$ ), and the dashed lines show the 95% credible interval ( $0.70^{\circ} - 1.23^{\circ}/\text{Myr}$ ). (C) Paleomagnetic poles generated using two distinct Euler poles. The first Euler pole is located at  $10^{\circ}\text{S}$ ,  $000^{\circ}\text{E}$  (blue star), and rotates at  $1.5^{\circ}/\text{Myr}$  for 60 Myr. The second Euler pole is located at  $10^{\circ}\text{N}$ ,  $300^{\circ}\text{E}$  (red star), and rotates at a speed of  $0.75^{\circ}/\text{Myr}$  for 60 Myr. The blue and red distributions show the posterior estimate location of the first and second Euler poles (respectively) recovered by the MCMC inversion. The blue and red arcs are 100 of the synthetic APWPs. (D) Posterior probability density for the rotation rates of the Euler poles recovered by the inversion. The solid lines show the median values of the distributions ( $\sim 1.45^{\circ}/\text{Myr}$  and  $0.76^{\circ}/\text{Myr}$  for Euler rotation 1 and 2), and the dashed lines show the 95% credible intervals.

450 poles and uniform prior distributions to the middle three (Fig. 5B). Despite this uninformative  
 451 prior distribution on the age of the middle three poles, the inversion successfully places the ages  
 452 of the middle three poles at *ca.* 115 Ma, *ca.* 90 Ma, and *ca.* 65 Ma as can be seen in their  
 453 posterior age distributions (Fig. 5D).

454 For real data, adding uncertainties to the ages of the poles enables us to properly represent our  
 455 knowledge of the constraints on the APWP. These uncertainties enable data to constrain the  
 456 location of the path without providing an overly tight constraint on the timing when the true age  
 457 is uncertain. The resulting posterior distributions provide predicted ages for the poles associated  
 458 with Euler pole inversions (Fig. 5D).

## 459 Reporting the apparent polar wander path

460 A difficulty with the Bayesian approach is that the credible interval of Euler pole solutions are  
 461 not easy to report as they do not neatly correspond to a parametric statistical distribution. We  
 462 visualize the solutions with spatial histograms for the Euler pole positions and by showing  
 463 example inverted paths. A typical product that one is seeking with such an inversion is an  
 464 apparent polar wander path reported as interpreted pole position at given intervals. An approach  
 465 that can be taken is to calculate a number of predicted pole positions at a given time implied by  
 466 inverted Euler pole models and then to calculate the Fisher mean of these inverted pole positions  
 467 as was done in Swanson-Hysell et al. (2019). This approach provides the mean pole position on  
 468 the apparent polar wander path. We also wish to report the uncertainty on that estimated  
 469 position. The spread in the position of these inverted pole positions has real meaning related to  
 470 the certainty of the position within the inversion that corresponds both to the best-fit in space  
 471 through the poles and that in time which affects the rate of the rotation about the Euler pole.  
 472 The spread in pole positions can be approximated as a Fisher distribution from which the angle  
 473 from the mean that contains 95% of the solutions ( $\theta_{95}$ ) can be calculated:

$$\theta_{95} = \frac{140^\circ}{\sqrt{\kappa}} \quad (21)$$

474 This angle is analogous to a  $2\sigma$  uncertainty in Gaussian statistics. Implied pole positions from  
 475 these inversions are more tightly clustered than the inverted Euler pole positions themselves and  
 476 typically are consistent with being drawn from a Fisher distribution such that reporting the 95%  
 477 confidence of angular deviation can be appropriate.

## 478 Application to the Keweenawan Track

479 An impetus for the development of this Bayesian paleomagnetic Euler pole inversion method was  
 480 to constrain the absolute rates of plate motion associated with the ca. 1109 to 1070 Ma  
 481 Keweenawan Track of paleomagnetic poles (Halls and Palmer, 1981; Swanson-Hysell et al., 2009,  
 482 2019). These poles are associated with the rapid motion of Laurentia towards the equator leading  
 483 up to the Grenvillian orogeny and the assembly of the supercontinent Rodinia (Swanson-Hysell,

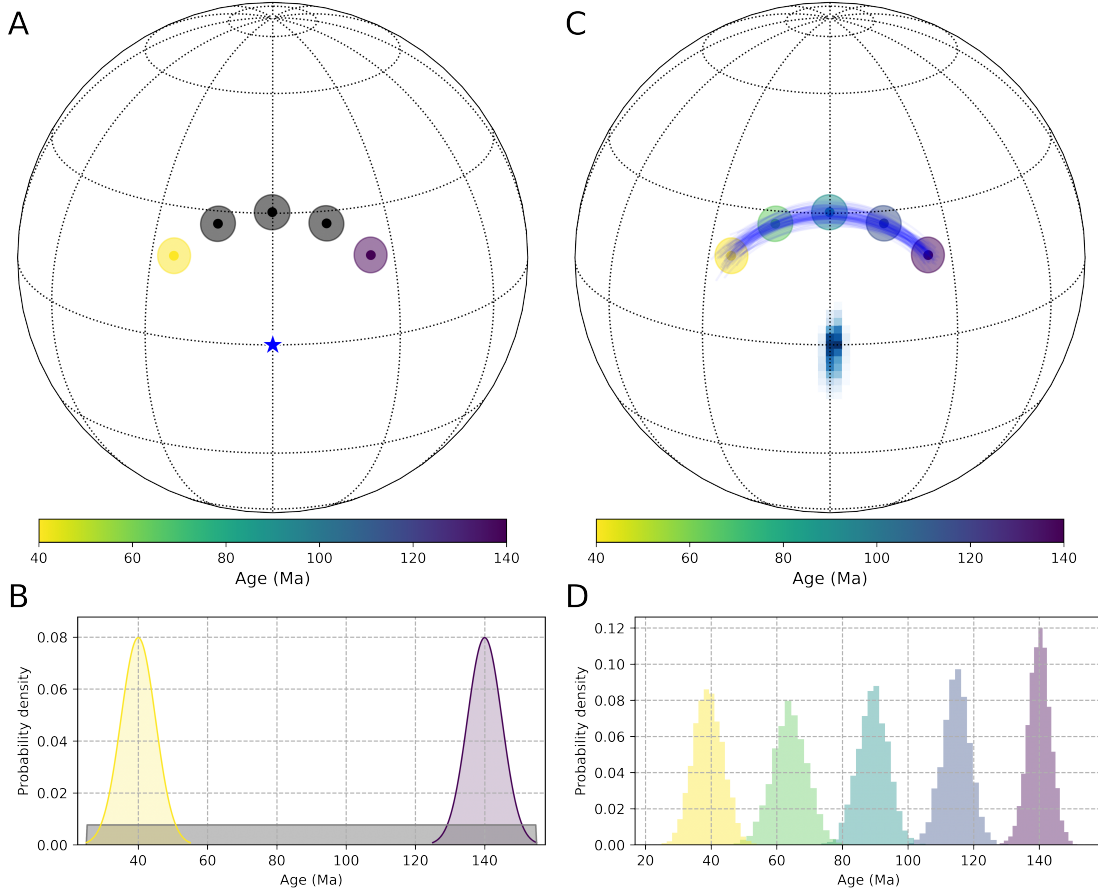


**Figure 5.** Synthetic data and one Euler pole inversion incorporating age uncertainty. (A, B) Assigned distributions associated with the paleomagnetic poles positions and ages. We take the first and last poles to be radiometrically dated with  $1\sigma$  uncertainties of 5 Myr such that they are assigned Gaussian prior distributions. The middle three poles are undated and constrained to be between the first and last poles with uniform probability. (C, D) Posterior distributions after 10<sup>5</sup> MCMC samples of the Euler pole position and pole ages. The posterior distributions for the age of the middle three poles are centered on their true values of 115 Ma, 90 Ma, and 65 Ma. The middle poles help constrain the location of the Euler pole, but with their wide uniform prior age distributions do little to constrain the rotation rate.

484 2021). While previous approaches had established estimates for the rate of latitudinal motion  
485 associated with the Keweenawan Track (Davis and Green, 1997; Swanson-Hysell et al., 2014), we  
486 implemented this Bayesian inversion method in Swanson-Hysell et al. (2019) in order to constrain  
487 absolute rates (without providing the level of detail on the methodology that is elucidated in the  
488 present contribution). In addition to our goals of constraining absolute rates, this approach was  
489 particularly appropriate for the Keweenawan Track as it includes poles with quite disparate  
490 precision on their age constraints as some are constrained tightly by high-precision U-Pb dates  
491 (e.g. Fairchild et al., 2017) while others have looser stratigraphic constraints. A technical note  
492 related to the analysis in Swanson-Hysell et al. (2019) is that it used a version of the code written  
493 in PyMC2 (Patil et al., 2010; <https://github.com/ian-r-rose/mcplates>). The PyMC project has  
494 migrated to PyMC3 which is a total rewrite of the module (Salvatier et al., 2016) and  
495 necessitated our code to refactored into its present PyMC3 version  
496 ([https://github.com/Swanson-Hysell-Group/Bayesian\\_PEP\\_inversion](https://github.com/Swanson-Hysell-Group/Bayesian_PEP_inversion)). These two versions of the  
497 code apply the same methodology and recover very similar solutions.

498 Paleomagnetic Euler pole inversions to the Keweenawan Track are shown in Fig. 6. The  
499 posterior distribution of the Euler pole positions are shown along with a sampling of the small  
500 circle paths generated from the posterior distribution which are plotted over the paleomagnetic  
501 poles. The prior distributions for the ages of the poles are shown in Fig. 6B as well as the  
502 posterior distribution of pole ages for the case of a one paleomagnetic Euler pole inversion. The  
503 prior probabilities assigned to the poles illustrate the variable age uncertainties associated with  
504 the paleomagnetic poles in the Keweenawan Track. The posterior distribution of the plate speed  
505 for Laurentia resulting from the inversions are shown along with their 95% credible intervals and  
506 are calculated in cm/yr for the position of Duluth, MN (46.8°N, 92.1°W). Applying a single  
507 paleomagnetic Euler pole inversion to the entirety of the Keweenawan Track results in a median  
508 rate of 30 cm/yr with a 95% credible interval of 27–34 cm/yr. Also shown in Figure 6 is an  
509 inversion with two Euler poles that results in a ca. 1096 Ma changepoint with rates that slow  
510 after the changepoint—a change that could be associated with the onset of collisional Grenvillian  
511 orogenesis. This two Euler pole inversion results in a significant improvement in fit as can be  
512 visualized by the modeled pole positions shown with the original pole positions in Figure 6A. In  
513 either case, estimated rates are significantly faster than the fastest Cenozoic plate speeds and  
514 above the 15 cm/yr threshold that Zahirovic et al. (2015) concludes requires exceptional  
515 explanation for plates with substantial continental lithosphere.

516 In the literature, the Keweenawan Track has variably be interpreted as being the result of fast  
517 differential plate motion (e.g. Davis and Green, 1997) or as the result of true polar wander (e.g.  
518 Evans, 2003). True polar wander results in rotations of the entire silicate Earth which means that  
519 such rotations result in great circle paths (Euler pole 90° from the path) and has the potential to  
520 progress at rapid rates (Rose and Buffett, 2017). Overall, true polar wander is a difficult signal to  
521 disentangle from plate motions, since any given APWP can be the result of true polar wander,  
522 plate tectonics, or some combination of the two. However, given the nature of a true polar wander  
523 rotation, an Euler pole that describes true polar wander must be 90° from the spin axis such that  
524 the Euler pole for a true polar wander event must be 90° from the paleomagnetic poles.  
525 Therefore, the extent to true polar wander could explain motion of the Keweenawan Track can be  
526 evaluated by constraining the location of the true polar wander Euler pole to be within a great

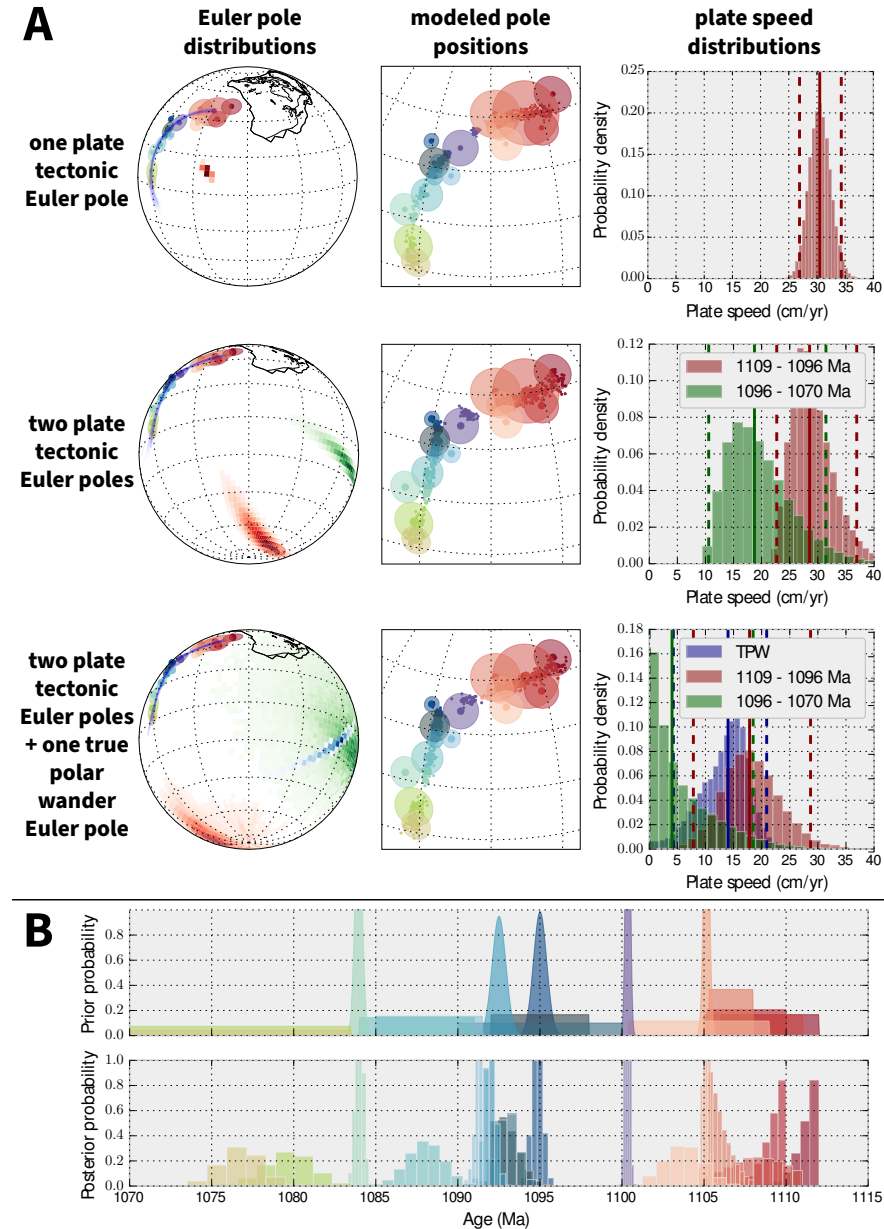


**Figure 6.** A) Bayesian paleomagnetic Euler pole inversion of the Keweenawan Track using three different combinations of Euler poles. The Euler pole locations and representative resulting tracks along with modeled pole positions are shown with the paleomagnetic poles. The distribution of plate speed associated with each inverted Euler pole is shown in the histograms with the 95% credible interval indicated with dashed lines. B) The upper plot illustrates the prior probability distributions for the ages of the paleomagnetic poles used in the inversion. Poles with radiometric ages are assigned Gaussian distributions while those with stratigraphic age control are assigned uniform distributions between bracketing ages. The posterior probability of poles ages resulting from the one plate tectonic Euler pole inversion are shown in the lower panel. See Swanson-Hysell et al. (2019) for details on individual paleomagnetic poles.

circle  $90^\circ$  from the path. This constraint can be imposed in the inversion by using a restrictive Watson girdle distribution. As shown in Swanson-Hysell et al. (2019), a single true polar wander rotation is a poor fit to the path given its curvature. However, the pole path could be the result of a combination of true polar wander and differential plate motion. This scenario can be explored through a model that inverts for a true polar wander Euler pole as well as differential plate tectonic Euler poles. A model wherein there is continuous true polar wander in addition to rapid plate motion that changes direction and slows ca. 1096 Ma is shown in Figure 6. While significant motion can be partitioned into true polar wander, significant plate motion remains with 97.5% of the solutions containing small circle plate tectonic motion that is faster than 20 cm/yr. This rapid motion is associated with subduction that led to the closure of the Unimos Ocean leading up to collisional Grenvillian orogenesis and the associated formation of the supercontinent Rodinia (Hynes and Rivers, 2010; Swanson-Hysell et al., 2022).

## Application to Australia's Cenozoic APWP

Australia and East Antarctica were connected from the Proterozoic until the Mesozoic when rifting led to the onset of seafloor spreading between the continents ca. 83 Ma (Williams et al., 2011; Veevers, 2012). This separation eventually resulted in the deep ocean Tasmanian Gateway which enabled the establishment of the Antarctic circumpolar current which is invoked as an important boundary condition that enabled the growth of large Antarctic ice sheets (Stickley et al., 2004).

Australia's plate motion relative to East Antarctica is considered to be well constrained from ca. 61 Ma to the present on the basis of fracture zones and magnetic anomaly data (Cande and Stock, 2004). The plate motion model of Müller et al. (2016) utilizes the reconstruction of Australia relative to East Antarctica of Cande and Stock (2004) for 38 Ma to the present-day and that of Whittaker et al. (2007) for 100 to 38 Ma. The absolute motion of Australia is constrained in the model through a plate circuit that reconstructs Australia relative to East Antarctica, East Antarctica relative to Africa, and Africa relative to the spin axis (Müller et al., 2016). In Figure 7, we show the implied pole position for Australia that results from this global plate motion model as well as rates. The model implies faster Euler rotation rates after 38 Ma than before that time associated with an acceleration in Australia's northward drift (Fig. 7D). We use these seafloor data based plate motion model as a comparison to an inversion of Cenozoic paleomagnetic data from Australia for the past 60 million years.

There is a contentious history of interpreting Australia's Cenozoic paleomagnetic record leading to varying APWPs with discussions of the relative fidelity of igneous and sedimentary poles in the literature (e.g. Idnurm, 1985; Musgrave, 1989; Idnurm, 1994; Hansma and Tohver, 2019). The paleomagnetic pole database for Australia in the Cenozoic has improved substantially with the development of both new Oligocene and Miocene paleomagnetic data (Hansma and Tohver, 2018, 2019) and Ar-Ar dates that provide ages for both previously undated units and supersede previous K-Ar dates (Cohen et al., 2008; Knesel et al., 2008; Cohen et al., 2013). This updated paleomagnetic pole database is listed in Table 1 and visualized in Figure 7A. These updated

Study/Region	Rock type	PLat	P Lon	A <sub>95</sub>	N	Pmag reference	Age (Ma)	Age min	Age max	Age information	Dist type
Holocene lake sediments	sedimentary	89.4	144.6	1.5	57	Idnurm (1985)	0.005	0	0.01	radiocarbon dates from Idnurm (1985)	uniform
Plio-Pleistocene mean	mixed	87.7	353	3.2	48	as in Hansma and Tohver (2019)	2	1	3	as compiled in Hansma and Tohver (2019)	uniform
Glenample Fm./Port Campbell Lst.	sedimentary	77.2	303.5	3.9	30	Idnurm (1985)	13	9	17	biostratigraphy from Dickinson et al. (2002)	uniform
Cosgrove leucite lavas	igneous	80.2	275.4	8.6	15	Hansma and Tohver (2018)	16	15	17	Ar-Ar dates with range assigned by Hansma and Tohver (2018)	uniform
Main Range Volcano	igneous	76.6	271.6	6.1	25	as in Hansma and Tohver (2019)	23.45	20.2	26.7	Ar-Ar dates from Knesel et al. (2008)	uniform
Tweed Volcano	igneous	77.4	306.9	5.4	48	as in Hansma and Tohver (2019)	23.9	23.1	24.7	Ar-Ar dates from Knesel et al. (2008)	uniform
Pt. Addis Limestone	sedimentary	68.5	299.4	4.8	4.8	Idnurm (1985)	25.1	22.4	27.8	Ar-Ar and biostratigraphic constraints from Idnurm (1985); McLaren et al. (2009)	uniform
Springsure Volcano	igneous	70.5	300.6	9.7	18	Hansma and Tohver (2019)	28.1	27.8	28.4	Ar-Ar date from Cohen et al. (2013)	normal
Peak Range	igneous	64.6	291.8	8.8	29	Hansma and Tohver (2019)	29.65	28.2	31.1	Ar-Ar dates from Cohen et al. (2013)	uniform
Hillsborough Volcano	igneous	67.1	301.4	7.1	14	Hansma and Tohver (2019)	33.6	33.1	34.1	Ar-Ar date from Cohen et al. (2013)	normal
Browns Creek Formation	sedimentary	65.5	292.5	2.5	33	Idnurm (1994)	35.5	36.2	34.9	biostratigraphy and magnetostratigraphy from Shafik and Idnurm (1997)	uniform
North Rankin Drill-core	sedimentary	61.7	298.4	5.1	20	Idnurm (1985)	59.75	57	62.5	foraminiferal zones P3 and P4 (ages of 62.5 to 57 in GTS 2020)	uniform

**Table 1.** Paleomagnetic poles and age constraints used for the Australia Cenozoic APWP inversion and associated references. PLat = pole latitude; PLon = pole longitude; A<sub>95</sub> = 95% angular confidence bounds on pole positions; N = number of site level VGP's used to calculate the mean pole positions; Pmag reference = reference for paleomagnetic pole data; Age (Ma) = nominal age calculated from age constraints on paleomagnetic poles; Age min = lower bounds for pole ages; Age max = upper bounds for pole ages; Age information = summary description for geochronology methods for pole ages and associated references; Dist type = choice of using uniform or normal distributions for assigning prior uncertainties for pole ages.

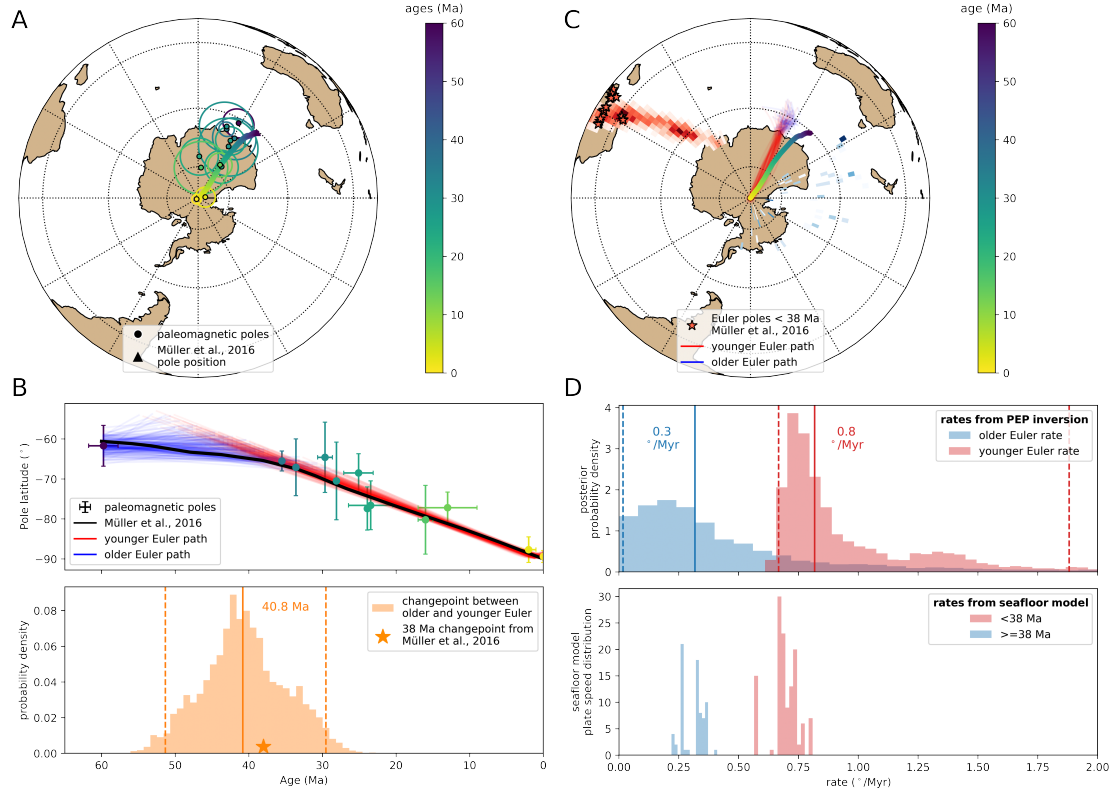


**Figure 7.** A) Cenozoic paleomagnetic poles for Australia used for the Bayesian inversion model are shown as circles with their  $A_{95}$  confidence ellipses colored by age. The continuous path using the same color scale is the implied pole position extracted from the Müller et al. (2016) seafloor-based model. B) The latitude of the pole position for the paleomagnetic poles is shown with their error bars. The black line is the latitude of the pole position implied by the Müller et al. (2016) model which undergoes a change in slope ca. 38 ma. The thin lines represent 100 of the pole paths resulting from the two Euler pole inversion with blue being the older path segment and red the younger segment. The lower histograms shows the posterior distribution of the age of changepoints from the older to younger Euler pole in the inversion. C) 100 sample oaths from the inversion shown in comparison to the Müller et al. (2016) path as well as density of the two inverted Euler poles is shown. Due to the low number of paleomagnetic poles between 60 Ma and the changepoint as well as the short length of the path, the position of the older Euler pole is not tightly constrained. The posterior distribution of the younger Euler pole position (red density on the globe) is more tightly constrained and coincides with the Euler poles (red stars) extracted from the global plate reconstruction model of Müller et al. (2016). D) The top panel shows the posterior distribution of the Euler rotation rates associated with the older and younger inverted Euler poles with the median shown with the solid line and the labeled rate. The lower panel is the Euler rotation rates for Australia extracted from the global plate reconstruction model before and after 38 Ma. There is a good correspondance between the median of the inversion posterior and the rates from the seafloor model.

566 paleomagnetic poles give us the opportunity to develop paleomagnetic Euler pole inversions that  
567 can be compared to the independent plate tectonic reconstruction of Müller et al. (2016).

568 The paleomagnetic data necessitate at least one change in the Euler pole between 60 Ma and  
569 the present. This need for multiple Euler poles is most readily visualized in the latitude of the  
570 poles which implies a change in rate between 60 Ma and the present (Fig. 7B). We apply the  
571 Bayesian inversion framework to invert for two Euler poles for Cenozoic Australia using prior  
572 probability constraints from these paleomagnetic poles. We use an uninformed prior probability  
573 for the timing of the changepoint between the two Euler poles in which it is assigned a uniform  
574 probability distribution between the age of the oldest ( $\sim 60$  Ma) and the youngest paleomagnetic  
575 poles ( $\sim 0.005$  Ma) in the compilation. The posterior distribution of the Euler pole positions,  
576 samples of the small circle paths generated from the posterior distributions, the implied pole  
577 latitudes, and the full plate motion angular rotation rates are shown in Figure 7. The inverted  
578 APWPs correspond well with the pole path from the Müller et al. (2016) model during the time  
579 interval where there is a higher concentration of paleomagnetic poles (ca. 35 Ma to the present;  
580 Fig. 7B,C). While the coverage of paleomagnetic poles is more sparse in the preceding time, the  
581 inversion is successful in recovering rates of motion and changes in this motion that are in  
582 agreement with the seafloor-based plate motion model (Fig. 7B,D). In particular, the inversion  
583 supports the interpretation that Australia's plate motion accelerated in the later portion of the  
584 Eocene. The posterior distributions for Euler rotation rates have median values that increase  
585 from  $0.3^\circ/\text{Myr}$  to  $0.8^\circ/\text{Myr}$  in agreement with the Müller et al. (2016) model (Fig. 7D). The 95%  
586 credible interval for the age of the changepoint associated with this change in rate spans from ca.  
587 51 to 30 Ma with a median 40.8 Ma. While this broad posterior distribution reflects the sparse  
588 constraints between 60 and 40 Ma, the timing of the change in rate is consistent with the Müller  
589 et al. (2016) model (Fig. 7B). In terms of the Euler pole positions, the shorter track length and  
590 the sparse paleomagnetic pole constraints result in the position of the older Euler pole being  
591 poorly resolved. In addition, the available ca. 60 Ma paleomagnetic pole does not imply the more  
592 eastward pole positions in the pole path ca. 60 Ma and instead has a position that agrees better  
593 with the previous seafloor data based model of Seton et al. (2012). In contrast, the younger Euler  
594 pole position is more tightly constrained through the inversion with the posterior distribution of  
595 the younger Euler pole positions (red density in Fig. 7B) concentrated near the Euler pole  
596 positions extracted from the Müller et al. (2016) model (red stars in Fig. 7C). Overall, the  
597 analysis highlights a broad agreement in the interpretation of kinematics that results from  
598 inversion of the Cenozoic paleomagnetic poles for Australia and that which results from  
599 seafloor-based plate motion models.

## 600 Conclusions

601 We have extended the paleomagnetic Euler pole analysis of Gordon et al. (1984) by placing it  
602 within a Bayesian framework. As a Bayesian inverse problem, Markov chain Monte Carlo  
603 (MCMC) numerical methods can be used to obtain estimates of Euler pole positions and rates as  
604 constrained by paleomagnetic poles. Regularization of the inversions is not accomplished by  
605 smoothing parameters, but can instead be accomplished through prior probability distributions

for the Euler pole parameters, which have clear physical interpretations. The approach enables uncertainties on both the positions and ages of paleomagnetic poles to be incorporated into the analysis. Any number of Euler poles can be included with the timing of changepoints between them being solved as part of the inversion. An advantage of this approach is that the paleomagnetic Euler poles provide an estimate for the total plate velocity including both latitudinal and relative longitudinal motion. The resulting posterior distributions from the inversions provide uncertainties for the model parameters – including estimates of plate velocity.

Challenges remain in the broad application of paleomagnetic Euler pole analysis. One set of challenges relates to the resolving power of the method. For slow rates of motion, the position of inverted Euler poles are uncertain and it is difficult to resolve the timing of changepoints with confidence. However, this issue is more related to the precision of available constraints and is the case regardless of method. The spread between resulting paths is much less than the spread of the posterior Euler pole position. Determining the number of change points to implement in an inversion is an additional challenge, and one that is also more difficult for slow motions or uncertain data. This issue is addressed theoretically in Gallo et al. (2021) who apply a frequentist approach to paleomagnetic Euler pole inversion and propose a graphical approach to evaluate for the optimal number of inverted Euler poles. The extension of such an approach to noisier suites of paleomagnetic data as well as integration with our Bayesian inversion approach could prove fruitful.

Overall, an advantage of paleomagnetic Euler pole analysis is that it utilizes a physical model of plate motions to inform the APWP shape that fits with our knowledge of plate motions. However, uncertainty remains regarding underlying assumptions including that Euler pole positions and associated plate motions are relatively stable over millions of years. Furthermore, the method also assumes that the timescale over which Euler pole positions themselves migrate are relatively rapid such that they can be approximated by instantaneous changepoints. Evaluating the validity of these assumptions is an area ripe for future research.

## Acknowledgements

This work was supported by National Science Foundation grants EAR-1246670 and EAR-1847277. We thank Bruce Buffett, David Evans, and Mike Tetley for useful discussions during development of the method. We thank Mat Domeier and members of the CEED YC2.0 workshop for informative discussions during the final writing of the manuscript. MCMC analysis was performed using PyMC3 (Salvatier et al., 2016). Additional analysis was performed using the Python packages NumPy (Harris et al., 2020), Scipy (Virtanen et al., 2020), and PmagPy (Tauxe et al., 2016). Figures were created using Matplotlib (Hunter, 2007) and Cartopy (Met Office, 2010 - 2015). The code implementing the analysis and developing the visualizations are documented within Jupyter notebooks (Kluyver et al., 2016) that are available on Github: [https://github.com/Swanson-Hysell-Group/Bayesian\\_PEP\\_inversion](https://github.com/Swanson-Hysell-Group/Bayesian_PEP_inversion).

## 643 References

- 644 Argus, D. F., Gordon, R. G., and DeMets, C., 2011, Geologically current motion of 56 plates relative to the  
645 no-net-rotation reference frame: *Geochemistry, Geophysics, and Geosystems*, vol. 12, doi:10.1029/2011gc003751.
- 646 Aster, R. C., Borchers, B., and Thurber, C. H., 2005, *Parameter estimation and inverse problems*: Elsevier.
- 647 Beck, J., Myrl E., 1989, Chapter 22: Paleomagnetism of continental North America; Implications for displacement  
648 of crustal blocks within the Western Cordillera, Baja California to British Columbia: *In* Pakiser, L. C. and  
649 Mooney, W. D., eds., *Geophysical Framework of the Continental United States*, Geological Society of America,  
650 vol. 172, doi:10.1130/MEM172-p471.
- 651 Beck, M. E. and Housen, B. A., 2003, Absolute velocity of North America during the Mesozoic from paleomagnetic  
652 data: *Tectonophysics*, vol. 377, pp. 33–54, doi:10.1016/j.tecto.2003.08.018.
- 653 Boyden, J. A., Müller, R. D., Gurnis, M., Torsvik, T. H., Clark, J. A., Turner, M., Ivey-Law, H., Watson, R. J., and  
654 Cannon, J. S., 2011, Next-generation plate-tectonic reconstructions using GPlates: *In* Baru, C. and Keller,  
655 G. R., eds., *Geoinformatics: Cyberinfrastructure for the Solid Earth Sciences*, Cambridge University Press,  
656 Cambridge, pp. 95–114, doi:10.1017/CBO9780511976308.008.
- 657 Bryan, P. and Gordon, R. G., 1986, Rotation of the Colorado Plateau: An analysis of paleomagnetic data:  
658 *Tectonics*, vol. 5, pp. 661–667, doi:10.1029/tc005i004p00661.
- 659 Bull, A. L., Domeier, M., and Torsvik, T. H., 2014, The effect of plate motion history on the longevity of deep  
660 mantle heterogeneities: *Earth and Planetary Science Letters*, vol. 401, pp. 172–182,  
661 doi:10.1016/j.epsl.2014.06.008.
- 662 Butler, R., 1992, *Paleomagnetism: Magnetic Domains to Geologic Terranes*: Blackwell Scientific Publications.
- 663 Cande, S. C. and Stock, J. M., 2004, Cenozoic reconstructions of the Australia-New Zealand-South Pacific sector of  
664 Antarctica: *In* The Cenozoic Southern Ocean: *Tectonics, Sedimentation, and Climate Change Between Australia*  
665 and Antarctica, American Geophysical Union, pp. 5–17, doi:10.1029/151gm02.
- 666 Carpenter, B., Gelman, A., Hoffman, M. D., Lee, D., Goodrich, B., Betancourt, M., Brubaker, M., Guo, J., Li, P.,  
667 and Riddell, A., 2017, Stan: A probabilistic programming language: *Journal of Statistical Software*, vol. 76, pp. 1  
668 – 32, doi:10.18637/jss.v076.i01.
- 669 Cohen, B. E., Knesel, K. M., Vasconcelos, P. M., and Schellart, W. P., 2013, Tracking the Australian plate motion  
670 through the Cenozoic: Constraints from  $^{40}\text{Ar}/^{39}\text{Ar}$  geochronology: *Tectonics*, vol. 32, pp. 1371–1383,  
671 doi:10.1002/tect.20084.
- 672 Cohen, B. E., Knesel, K. M., Vasconcelos, P. M., Thiede, D. S., and Hergt, J. M., 2008,  $^{40}\text{Ar}/^{39}\text{Ar}$  constraints on  
673 the timing and origin of Miocene leucite volcanism in southeastern Australia: *Australian Journal of Earth*  
674 *Sciences*, vol. 55, pp. 407–418, doi:10.1080/08120090701769514.
- 675 Cox, A. and Hart, R., 2009, *Plate Tectonics: How It Works*: Wiley.
- 676 Davidson-Pilon, C., 2015, *Bayesian Methods for Hackers: Probabilistic Programming and Bayesian Inference*:  
677 Addison-Wesley.
- 678 Davis, D. and Green, J., 1997, Geochronology of the North American Midcontinent rift in western Lake Superior  
679 and implications for its geodynamic evolution: *Canadian Journal of Earth Science*, vol. 34, pp. 476–488,  
680 doi:10.1139/e17-039.
- 681 DeMets, C., Gordon, R. G., and Argus, D. F., 2010, Geologically current plate motions: *Geophysical Journal*  
682 *International*, vol. 181, pp. 1–80, doi:10.1111/j.1365-246x.2009.04491.x.

- 683 Dickinson, J. A., Wallace, M. W., Holdgate, G. R., Gallagher, S. J., and Thomas, L., 2002, Origin and timing of the  
684 Miocene-Pliocene Unconformity in southeast Australia: *Journal of Sedimentary Research*, vol. 72, pp. 288–303,  
685 doi:10.1306/082701720288.
- 686 Evans, D. A. D., 2003, True polar wander and supercontinents: *Tectonophysics*, vol. 362, pp. 303–320,  
687 doi:10.1016/S0040-1951(02)000642-X.
- 688 Fairchild, L. M., Swanson-Hysell, N. L., Ramezani, J., Sprain, C. J., and Bowring, S. A., 2017, The end of  
689 Midcontinent Rift magmatism and the paleogeography of Laurentia: *Lithosphere*, vol. 9, pp. 117–133,  
690 doi:10.1130/L580.1.
- 691 Fisher, N. I., Lewis, T., and Embleton, B. J. J., 1987, *Statistical Analysis of Spherical Data*: Cambridge University  
692 Press, doi:10.1017/CBO9780511623059.
- 693 Forsyth, D. and Uyeda, S., 1975, On the relative importance of the driving forces of plate motion: *Geophysical  
694 Journal International*, vol. 43, pp. 163–200, doi:10.1111/j.1365-246X.1975.tb00631.x.
- 695 Forte, A. M. and Peltier, W. R., 1987, Plate tectonics and aspherical earth structure: The importance of  
696 poloidal-toroidal coupling: *Journal of Geophysical Research: Solid Earth*, vol. 92, p. 3645,  
697 doi:10.1029/jb092ib05p03645.
- 698 Francheteau, J. and Sclater, J. G., 1969, Paleomagnetism of the southern continents and plate tectonics: *Earth and  
699 Planetary Science Letters*, vol. 6, pp. 93–106, doi:10.1016/0012-821X(69)90126-5.
- 700 Gable, C. W., O'Connell, R. J., and Travis, B. J., 1991, Convection in three dimensions with surface plates:  
701 Generation of toroidal flow: *Journal of Geophysical Research: Solid Earth*, vol. 96, p. 8391,  
702 doi:10.1029/90jb02743.
- 703 Gallo, L., Sapienza, F., and Domeier, M., 2021, An optimization method for paleomagnetic Euler pole analysis:  
704 *EarthArxiv*, doi:10.31223/X58900.
- 705 Gelman, A., Carlin, J. B., Stern, H. S., and Rubin, D. B., 2013, *Bayesian Data Analysis*: Chapman and Hall.
- 706 Gelman, A. and Rubin, D. B., 1996, Markov chain Monte Carlo methods in biostatistics: *Statistical Methods in  
707 Medical Research*, vol. 5, pp. 339–355, doi:10.1177/096228029600500402.
- 708 Goldstein, H., 1965, *Classical mechanics*: Pearson.
- 709 Gordon, R. G., Cox, A., and Harter, C. E., 1978, Absolute motion of an individual plate estimated from its ridge  
710 and trench boundaries: *Nature*, vol. 274, pp. 752–755, doi:10.1038/274752a0.
- 711 Gordon, R. G., Cox, A., and O'Hare, S., 1984, Paleomagnetic Euler poles and the apparent polar wander and  
712 absolute motion of North America since the Carboniferous: *Tectonics*, vol. 3, pp. 499–537,  
713 doi:10.1029/TC003i005p00499.
- 714 Halls, H. and Palmer, H., 1981, Remagnetization in Keweenawan rocks. Part II: lava flows within the Copper  
715 Harbor Conglomerate, Michigan: *Canadian Journal of Earth Science*, vol. 18.
- 716 Hansma, J. and Tohver, E., 2018, Palaeomagnetism of mid-Miocene leucitite volcanics in eastern Australia:  
717 *Geophysical Journal International*, vol. 215, pp. 303–313, doi:10.1093/gji/ggy281.
- 718 Hansma, J. and Tohver, E., 2019, Paleomagnetism of Oligocene hot spot volcanics in central Queensland, Australia:  
719 *Journal of Geophysical Research: Solid Earth*, vol. 124, pp. 6280–6296, doi:10.1029/2019jb017639.
- 720 Harris, C. R., Millman, K. J., van der Walt, S. J., Gommers, R., Virtanen, P., Cournapeau, D., Wieser, E., Taylor,  
721 J., Berg, S., Smith, N. J., Kern, R., Picus, M., Hoyer, S., van Kerkwijk, M. H., Brett, M., Haldane, A., del Río,  
722 J. F., Wiebe, M., Peterson, P., Gérard-Marchant, P., Sheppard, K., Reddy, T., Weckesser, W., Abbasi, H.,  
723 Gohlke, C., and Oliphant, T. E., 2020, Array programming with Numpy: *Nature*, vol. 585, pp. 357–362,  
724 doi:10.1038/s41586-020-2649-2.

- 725 Hunter, J. D., 2007, Matplotlib: A 2D graphics environment: Computing in Science & Engineering, vol. 9, pp.  
726 90–95, doi:10.1109/MCSE.2007.55.
- 727 Hynes, A. and Rivers, T., 2010, Protracted continental collision — evidence from the Grenville Orogen: Canadian  
728 Journal of Earth Sciences, vol. 47, pp. 591–620, doi:10.1139/e10-003.
- 729 Iaffaldano, G., Bodin, T., and Sambridge, M., 2012, Reconstructing plate-motion changes in the presence of  
730 finite-rotations noise: Nature Communications, vol. 3, p. 1048, doi:10.1038/ncomms2051.
- 731 Idnurm, M., 1985, Late Mesozoic and Cenozoic palaeomagnetism of Australia – I. A redetermined apparent polar  
732 wander path: Geophysical Journal International, vol. 83, pp. 399–418, doi:10.1111/j.1365-246x.1985.tb06494.x.
- 733 Idnurm, M., 1994, New late Eocene pole for Australia, time-averaging of remanence directions, and  
734 palaeogeographic reference systems: Geophysical Journal International, vol. 117, pp. 827–833,  
735 doi:10.1111/j.1365-246x.1994.tb02473.x.
- 736 Irving, E., 1977, Drift of the major continental blocks since the Devonian: Nature, vol. 270, pp. 304–309,  
737 doi:10.1038/270304a0.
- 738 Irving, E. and Park, J. K., 1972, Hairpins and superintervals: Canadian Journal of Earth Sciences, vol. 9, pp.  
739 1318–1324, doi:10.1139/e72-115.
- 740 Jupp, P. E. and Kent, J. T., 1987, Fitting smooth paths to spherical data: Journal of the Royal Statistical Society.  
741 Series C (Applied Statistics), vol. 36, pp. 34–46, doi:10.2307/2347843.
- 742 Kluyver, T., Ragan-Kelley, B., Pérez, F., Granger, B., Bussonnier, M., Frederic, J., Kelley, K., Hamrick, J., Grout,  
743 J., Corlay, S., and Ivanov, P., 2016, Jupyter notebooks – a publishing format for reproducible computational  
744 workflows: In Positioning and Power in Academic Publishing: Players, Agents and Agendas, IOS Press,  
745 doi:10.3233/978-1-61499-649-1-87.
- 746 Knesel, K. M., Cohen, B. E., Vasconcelos, P. M., and Thiede, D. S., 2008, Rapid change in drift of the Australian  
747 plate records collision with Ontong Java plateau: Nature, vol. 454, pp. 754–757, doi:10.1038/nature07138.
- 748 Lunn, D. J., Thomas, A., Best, N., and Spiegelhalter, D., 2000, WinBUGS - A Bayesian modelling framework:  
749 Concepts, structure, and extensibility: Statistics and Computing, vol. 10, pp. 325–337,  
750 doi:10.1023/A:1008929526011.
- 751 McLaren, S., Sandiford, M., Dunlap, W. J., Scrimgeour, I., Close, D., and Edgoose, C., 2009, Distribution of  
752 Palaeozoic reworking in the Western Arunta Region and northwestern Amadeus Basin from  $^{40}\text{Ar}/^{39}\text{Ar}$   
753 thermochronology: implications for the evolution of intracratonic basins: Basin Research, vol. 21, pp. 315–334.
- 754 McNamara, A. K. and Zhong, S., 2005, Thermochemical structures beneath Africa and the Pacific Ocean: Nature,  
755 vol. 437, pp. 1136–1139, doi:10.1038/nature04066.
- 756 Met Office, 2010 - 2015, Cartopy: a cartographic python library with a matplotlib interface: Exeter, Devon, URL  
757 <http://scitools.org.uk/cartopy>.
- 758 Minson, S. E., Simons, M., and Beck, J. L., 2013, Bayesian inversion for finite fault earthquake source models  
759 I—theory and algorithm: Geophysical Journal International, vol. 194, pp. 1701–1726, doi:10.1093/gji/ggt180.
- 760 Muller, R., Royer, J.-Y., and Lawver, L., 1993, Revised plate motions relative to the hotspots from combined  
761 Atlantic and Indian Ocean hotspot tracks: Geology, vol. 21, pp. 275–278,  
762 doi:10.1130/0091-7613(1993)021<0275:RPMRTT>2.3.CO;2.
- 763 Müller, R. D., Seton, M., Zahirovic, S., Williams, S. E., Matthews, K. J., Wright, N. M., Shephard, G. E., Maloney,  
764 K. T., Barnett-Moore, N., Hosseinpour, M., and et al., 2016, Ocean basin evolution and global-scale plate  
765 reorganization events since pangea breakup: Annual Review of Earth and Planetary Sciences, vol. 44, pp.  
766 107–138, doi:10.1146/annurev-earth-060115-012211.

- 767 Musgrave, R. J., 1989, A weighted least-squares fit of the Australian apparent polar wander path for the last 100  
768 Myr: *Geophysical Journal International*, vol. 96, pp. 231–243, doi:10.1111/j.1365-246x.1989.tb04447.x.
- 769 Patil, A., Huard, D., and Fonnesbeck, C. J., 2010, PyMC: Bayesian stochastic modelling in Python: *Journal of*  
770 *Statistical Software*, vol. 35, pp. 1–81.
- 771 Richardson, R. M., 1992, Ridge forces, absolute plate motions, and the intraplate stress field: *Journal of*  
772 *Geophysical Research: Solid Earth*, vol. 97, p. 11,739, doi:10.1029/91jb00475.
- 773 Rose, I. and Buffett, B., 2017, Scaling rates of true polar wander in convecting planets and moons: *Physics of the*  
774 *Earth and Planetary Interiors*, doi:10.1016/j.pepi.2017.10.003.
- 775 Salvatier, J., Wiecki, T. V., Fonnesbeck, C., and Elkan, C., 2016, Probabilistic programming in Python using  
776 PyMC3: *PeerJ Computer Science*, vol. 2, p. e55, doi:10.7717/peerj-cs.55.
- 777 Sambridge, M., Bodin, T., Gallagher, K., and Tkalcic, H., 2013, Transdimensional inference in the geosciences:  
778 *Philosophical Transactions of the Royal Society A: Mathematical, Physical and Engineering Sciences*, vol. 371,  
779 doi:10.1098/rsta.2011.0547.
- 780 Seton, M., Müller, R. D., Zahirovic, S., Gaina, C., Torsvik, T., Shephard, G., Talsma, A., Gurnis, M., Turner, M.,  
781 Maus, S., and Chandler, M., 2012, Global continental and ocean basin reconstructions since 200 Ma:  
782 *Earth-Science Reviews*, vol. 113, pp. 212–270, doi:10.1016/j.earscirev.2012.03.002.
- 783 Shafik, S. and Idnurm, M., 1997, Calcareous microplankton and polarity reversal stratigraphies of the upper Eocene  
784 browns creek clay in the Otway Basin, southeast Australia: Matching the evidence: *Australian Journal of Earth*  
785 *Sciences*, vol. 44, pp. 77–86, doi:10.1080/08120099708728295.
- 786 Sivia, D. and Skilling, J., 2006, *Data Analysis: A Bayesian Tutorial*: Oxford University Press.
- 787 Smirnov, A. V. and Tarduno, J. A., 2010, Co-location of eruption sites of the Siberian Traps and North Atlantic  
788 Igneous Province: Implications for the nature of hotspots and mantle plumes: *Earth and Planetary Science*  
789 *Letters*, vol. 297, pp. 687–690, doi:10.1016/j.epsl.2010.07.023.
- 790 Stickley, C. E., Brinkhuis, H., Schellenberg, S. A., Sluijs, A., Röhl, U., Fuller, M., Grauert, M., Huber, M.,  
791 Warnaar, J., and Williams, G. L., 2004, Timing and nature of the deepening of the Tasmanian Gateway:  
792 *Paleoceanography*, vol. 19, doi:10.1029/2004pa001022.
- 793 Swanson-Hysell, N. L., 2021, The Precambrian Paleogeography of Laurentia: *In* Pesonen, L. J., Evans, D. A. D.,  
794 Elming, S. Å., Salminen, J. M., and Veikkolainen, T., eds., *Ancient Supercontinents and the Paleogeography of*  
795 *the Earth*, Elsevier, pp. 109–153, doi:10.1016/B978-0-12-818533-9.00009-6.
- 796 Swanson-Hysell, N. L., Maloof, A. C., Weiss, B. P., and Evans, D. A. D., 2009, No asymmetry in geomagnetic  
797 reversals recorded by 1.1-billion-year-old Keweenawan basalts: *Nature Geoscience*, vol. 2, pp. 713–717,  
798 doi:10.1038/ngeo622.
- 799 Swanson-Hysell, N. L., Ramezani, J., Fairchild, L. M., and Rose, I. R., 2019, Failed rifting and fast drifting:  
800 Midcontinent Rift development, Laurentia's rapid motion and the driver of Grenvillian orogenesis: *GSA Bulletin*,  
801 vol. 131, pp. 913–940, doi:10.1130/b31944.1.
- 802 Swanson-Hysell, N. L., Rivers, T., and van der Lee, S., 2022, The late Mesoproterozoic to early Neoproterozoic  
803 Grenvillian Orogeny and the assembly of Rodinia: Turning point in the tectonic evolution of Laurentia: *In*  
804 Whitmeyer, S., Kellett, D., Tikoff, B., and Williams, M., eds., *Laurentia: Evolution of a Continent*, Geological  
805 Society of America Memoir.
- 806 Swanson-Hysell, N. L., Vaughan, A. A., Mustain, M. R., and Asp, K. E., 2014, Confirmation of progressive plate  
807 motion during the Midcontinent Rift's early magmatic stage from the Osler Volcanic Group, Ontario, Canada:  
808 *Geochemistry Geophysics Geosystems*, vol. 15, pp. 2039–2047, doi:10.1002/2013GC005180.

- 809 Tarduno, J. A., McWilliams, M., and Sleep, N., 1990, Fast instantaneous oceanic plate velocities recorded by the  
810 Cretaceous Laytonville limestone: Paleomagnetic analysis and kinematic implications: *Journal of Geophysical*  
811 *Research-Solid Earth*, vol. 95, p. 15,503, doi:10.1029/jb095ib10p15503.
- 812 Tarling, D. H. and Abdeldayem, A. L., 1996, Palaeomagnetic-pole errors and a ‘small-circle’ assessment of the  
813 Gondwanan polar-wander path: *Geophysical Journal International*, vol. 125, pp. 115–122,  
814 doi:10.1111/j.1365-246X.1996.tb06538.x.
- 815 Tauxe, L., 2010, *Essentials of Paleomagnetism*: University of California Press.
- 816 Tauxe, L., Shaar, R., Jonestrask, L., Swanson-Hysell, N., Minnett, R., Koppers, A., Constable, C., Jarboe, N.,  
817 Gaastra, K., and Fairchild, L., 2016, PmagPy: Software package for paleomagnetic data analysis and a bridge to  
818 the Magnetics Information Consortium (MagIC) Database: *Geochemistry, Geophysics, Geosystems*, vol. 17, pp.  
819 2450–2463, doi:10.1002/2016GC006307.
- 820 Torsvik, T., Smethurst, M., Meert, J., Van der Voo, R., McKerrow, W., Brasier, M., Sturt, B., and Walderhaug, H.,  
821 1996, Continental break-up and collision in the Neoproterozoic and Paleozoic – A tale of Baltica and Laurentia:  
822 *Earth-Science Reviews*, vol. 40, pp. 229–258, doi:10.1016/0012-8252(96)00008-6.
- 823 Torsvik, T. H., Müller, R. D., Van der Voo, R., Steinberger, B., and Gaina, C., 2008, Global plate motion frames:  
824 Toward a unified model: *Reviews of Geophysics*, vol. 46, p. RG3004, doi:10.1029/2007RG000227.
- 825 Torsvik, T. H., Smethurst, M. A., Van der Voo, R., Trench, A., Abrahamsen, N., and Halvorsen, E., 1992, Baltica.  
826 A synopsis of Vendian-Permian palaeomagnetic data and their palaeotectonic implications: *Earth-Science*  
827 *Reviews*, vol. 33, pp. 133–152, doi:10.1016/0012-8252(92)90023-M.
- 828 Van der Voo, R., 1990, The reliability of paleomagnetic data: *Tectonophysics*, vol. 184, pp. 1–9,  
829 doi:10.1016/0040-1951(90)90116-P.
- 830 Van der Voo, R. and Torsvik, T., 2001, Evidence for late Paleozoic and Mesozoic non-dipole fields provides an  
831 explanation for the Pangea reconstruction problems: *Earth and Planetary Science Letters*, vol. 187, pp. 71–81,  
832 doi:10.1016/S0012-821X(01)00285-0.
- 833 Veevers, J., 2012, Reconstructions before rifting and drifting reveal the geological connections between Antarctica  
834 and its conjugates in Gondwanaland: *Earth-Science Reviews*, vol. 111, pp. 249–318,  
835 doi:10.1016/j.earscirev.2011.11.009.
- 836 Virtanen, P., Gommers, R., Oliphant, T. E., Haberland, M., Reddy, T., Cournapeau, D., Burovski, E., Peterson, P.,  
837 Weckesser, W., Bright, J., van der Walt, S. J., Brett, M., Wilson, J., Millman, K. J., Mayorov, N., Nelson, A.  
838 R. J., Jones, E., Kern, R., Larson, E., Carey, C. J., Polat, İ., Feng, Y., Moore, E. W., VanderPlas, J., Laxalde,  
839 D., Perktold, J., Cimrman, R., Henriksen, I., Quintero, E. A., Harris, C. R., Archibald, A. M., Ribeiro, A. H.,  
840 Pedregosa, F., van Mulbregt, P., and SciPy 1.0 Contributors, 2020, SciPy 1.0: Fundamental Algorithms for  
841 Scientific Computing in Python: *Nature Methods*, vol. 17, pp. 261–272, doi:10.1038/s41592-019-0686-2.
- 842 Whittaker, J. M., Müller, R. D., Leitchenkov, G., Stagg, H., Sdrolias, M., Gaina, C., and Goncharov, A., 2007,  
843 Major Australian-Antarctic plate reorganization at Hawaiian-Emperor bend time: *Science*, vol. 318, pp. 83–86,  
844 doi:10.1126/science.1143769.
- 845 Williams, S. E., Whittaker, J. M., and Müller, R. D., 2011, Full-fit, palinspastic reconstruction of the conjugate  
846 Australian-Antarctic margins: *Tectonics*, vol. 30, doi:10.1029/2011tc002912.
- 847 Zahirovic, S., Müller, R. D., Seton, M., and Flament, N., 2015, Tectonic speed limits from plate kinematic  
848 reconstructions: *Earth and Planetary Science Letters*, vol. 418, pp. 40–52, doi:10.1016/j.epsl.2015.02.037.